J. Fluid Mech. (2024), *vol*. 998, A49, doi:10.1017/jfm.2024.444

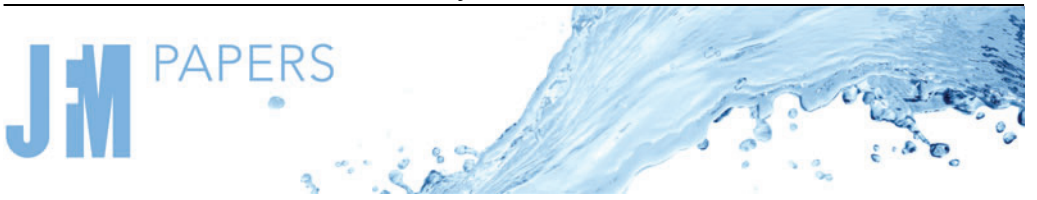

Pseudosteady shock refractions over an air–water interface

C. Anbu Serene Raj[1], **S. Vishnu Prasad**[1], **G. Rajesh**[1,†] **and A. Sameen**[1]

[1]Department of Aerospace Engineering, Indian Institute of Technology Madras, Chennai 600036, India

(Received 10 January 2024; revised 25 April 2024; accepted 28 April 2024)

Shock refraction in a gas–liquid interface is ubiquitous in nature and engineering. This study investigates the shock refraction phenomena in air–water interfaces for various inclination angles. The interface inclination angles are achieved using a tiltable vertical shock tube. The time-resolved schlieren images are compared with numerical simulations performed using the BlastFoam solver in the OpenFOAM software. The stiffened gas equation of state is used to model water in the simulations. The shock polar analysis using modified shock relations for a stiffened gas is used to elucidate the refraction patterns. A regular refraction pattern with a reflected shock wave and a bound precursor refraction with a regular reflection are observed experimentally for the first time in an air–water system. Further, a new free precursor refraction pattern with a Mach reflection is observed. The transition criteria and the corresponding boundaries for each refraction pattern are demarcated in the (M_S, θ_w^c)-plane. The refraction sequence and the range for various incident shock strength regimes are also identified.

Key words: shock waves, gas dynamics, multiphase flow

1. Introduction

A shock wave moving through a compressible medium reflects off with zero or very little transmission when it encounters a solid boundary. In comparison, the interaction of a shock wave with an interface separating two fluids of different densities can create interesting flow features and shock dynamics owing to significant transmission into the second fluid apart from its reflection at the interface. This interaction can be analysed in two distinct time periods. When the shock wave comes in contact with the interface during the initial times, the refraction phenomena dominate the problem, where the shock wave undergoes a change in its direction and intensity due to the variation in the acoustic impedance from one medium to the other. The class of studies dealing with such

† Email address for correspondence: rajesh@ae.iitm.ac.in

phenomena is called the shock-refraction problems, where inviscid Euler equations are known to govern the dynamics.

At a later period, once the shock traverses over the interface, the resulting entrainment, instability development and turbulent mixing come into play. The instability associated with the shock impingement on a usually perturbed interface is the celebrated Richtmyer–Meshkov instability (RMI) (Richtmyer 1960; Meshkov 1969). Misalignment of pressure and density gradients, quantified by the baroclinic vorticity, drives this interfacial instability. The RMI development in inclined interfaces has also been studied in detail over the years (refer to McFarland *et al.* (2013) and Luo *et al.* (2016)). The present work focuses on the initial time period when there is refraction of the shock wave on the interface and not the ensuing interfacial instability (the RMI).

The refracting media can be of the same phase or two different phases. The interface is called a slow–fast interface when the speed of sound is faster in the second medium where the transmitted wave travels and *vice versa* for a fast–slow interface. Shock refraction studies in gas–gas interfaces started with the pioneering works of Polachek & Seeger (1951), who suggested analytical expressions for a regular refraction wave system. Regular refraction is a three-wave system similar to its reflection counterpart, referred to as RR (Ben-Dor 2007), with the addition of a transmitted wave in the second medium. In regular refraction, all three waves are locally straight and intersect at a single point on the interface. Two types of regular refraction wave systems were identified by Polachek & Seeger (1951): regular refraction with a reflected shock wave (RRR) and regular refraction with a reflected expansion wave. Jahn (1956) verified these refraction patterns experimentally and observed other irregular refraction patterns. Irregular refraction systems are those comprising more than three waves. Henderson (1966) gave analytical explanations for these refraction patterns in both slow–fast and fast–slow interfaces using shock polars. Shock polars are graphical representations of the Rankine–Hugoniot equations in the pressure ratio-flow deflection angle plane (Keith & John 2006). Abd-El-Fattah & Henderson (1976, 1978*a*,*b*) classified the refractions in fast–slow and slow–fast interface groups into subclasses based on the incident shock strength. They identified four subclasses in fast–slow interfaces: very weak; weak; strong; and stronger incident shocks. Further, three subclasses were identified in slow–fast interfaces: very weak; weak; and strong incident shocks.

Henderson (1989) included the acoustic impedance in the boundary conditions of the analytical expressions for the oblique shock refractions in the gas–gas interfaces, where the acoustic impedance is a function of density and speed of sound of the medium. He also studied the transition from one refraction pattern to another in a slow–fast interface by increasing the angle between the incident shock and the contact discontinuity (Henderson, Colella & Puckett 1991). Zeng & Takayama (1996) experimentally and computationally verified the above transition conditions of refraction patterns in a slow–fast interface. Henderson, Puckett & Colella (2004) extended his earlier studies and numerically identified additional five anomalous refraction patterns, comprising at least five refracting shocks. From the above studies, the current understanding of shock refraction in a gas–gas interface indicates 12 known distinct patterns, eight in slow–fast and four in fast–slow interfaces. These patterns are corroborated by various later numerical studies (Nourgaliev *et al.* 2005; Delmont, Keppens & Van der Holst 2009).

Similar to gas–gas interfaces, shock refraction analysis can be extended to two-phase interfaces, which can either be a liquid–gas (fast–slow) or a gas–liquid (slow–fast) interfaces. A typical fast–slow multiphase interface is that of a water–air interface, where the shock wave originates from the medium with a higher acoustic impedance (water).

Such a situation can arise during an underwater explosion or a shock-induced bubble collapse. The refraction patterns resulting from such shock-interface interactions are distinct compared with those from a slow–fast interface, such as the situation discussed in this paper. Only strong incident shocks are possible in water–air interfaces, and the refraction patterns have been analysed by only a handful of studies, including those of Menikoff & Grove (1990) and Nourgaliev *et al.* (2005). The two refraction patterns identified in the above studies are (i) regular refraction with a reflected expansion wave and (ii) concave-forwards irregular refraction or an anomalous refraction with a reflected expansion. A more recent study by Xiang & Wang (2019) numerically and theoretically investigated the above refraction pattern transitions and gave analytical solutions to pressure ratio and flow Mach number behind the transmitted wave. It should be noted here that the water is modelled in their study using Tait's equation of state.

The current study of shock refraction is on the air–water system corresponding to a multiphase slow–fast interface. Shock refraction on an air–water interface can occur in wide engineering and medical applications. For example, in supersonic combustors, shocks interact with fuel droplets. In ballistics, detonation over an ocean surface or an explosion in a partially filled liquid tank can cause a spherical blast wave to interact with the liquid interface. In medicinal applications such as shock wave lithotripsy, focused shock waves are used to treat kidney stones. These extracorporeal shocks pass through bodily fluids with different acoustic impedances, resulting in various shock refraction patterns.

The phenomenon of a shock interacting with a gas–liquid interface can be classified into three categories: (i) a plane shock wave sliding over a horizontal liquid interface ($\beta = 90^\circ$); (ii) a plane shock wave interacting with an oblique liquid interface ($0^\circ \leq \beta < 90^\circ$); (iii) a curved shock wave interacting with a plane liquid surface or a plane shock wave interacting with a curved interface or a curved shock wave interacting with a curved liquid surface, where β varies continuously with time. Here, β is the angle between the shock wave and the interface. The first category focuses on the liquid surface entrainment due to Kelvin–Helmholtz instability created by the passage of the shock front (Rodriguez *et al.* 2016), specifically at $\beta = 90^\circ$. Such shock-induced mixing is important for its applications in high-speed combustion (Borison *et al.* 1981). The second category is where the interface is at a constant oblique angle $\beta \neq 90^\circ$, while the shock wave is planar and moving at a constant shock Mach number, M_S. Such problems are pseudosteady in nature (Ben-Dor 2007). The third category is an unsteady problem where the shock inclination β and/or the shock strength change continuously, creating different reflection patterns through shock transitions (Borisov, Kogarko & Lyubimov 1965; Hosseini *et al.* 2014; Sembian *et al.* 2016; Xiang & Wang 2017; Arun Kumar, Rajesh & Jagadeesh 2022). An example of such an unsteady phenomenon is when a blast wave interacts with a water column. A recent study by Wang, Zhai & Luo (2022) classifies and illustrates such unsteady shock reflections from a solid wedge into 10 different types. However, to understand and classify such an unsteady phenomenon at a multiphase interface, the second category discussed above is fundamental, and the literature available on such shock refractions is minimal (to the best of our knowledge).

Owing to the considerable impedance mismatch between a gas and a liquid, shock refraction has similarities with the shock reflection from solid surfaces. Takayama & Ben-Dor (1989) conducted experiments on the shock reflection phenomena from an oblique air–water interface (water wedge). They were motivated to use a water wedge because the RR to Mach reflection (MR) transition on solid wedge flows was affected significantly by the boundary layer developed just behind the incident shock. They found

that the transition angles agreed well with the detachment criterion (Ben-Dor 2007) for a specific range of shock Mach numbers (M_S). For $M_S < 1.47$, however, the match between theoretical and experimental transition angles was poor. It should be noted that the authors were interested in studying only the reflection, not the refraction patterns. Henderson *et al.* (1990) used impedance relations to calculate the reflection and transmission coefficients for an air–water interface along with the modified Tait equation (Dymond & Malhotra 1988). They experimented with a tilted shock tube and validated the refraction patterns against the numerical results. Nourgaliev *et al.* (2005) computationally simulated the shock refraction patterns for both liquid–gas and gas–liquid interfaces. They reported that unlike in gas–gas interfaces, a bound precursor refraction (BPR) was absent in the air–water interface. The refraction sequence for an air–water interface in the very weak incident shock regime was summarised to be RRR $\rightarrow$ FPR $\rightarrow$ FNR (free precursor refraction with a regular reflection (FPR) and free precursor von Neumann refraction (FNR)).

Recently, Wan *et al.* (2017) performed high-resolution numerical simulations of air–water interface for shock Mach numbers up to 4 and compared the transition angles from RR with irregular reflection and the triple point trajectories with solid wedge cases. They also experimented with an inclined shock tube for $M_S < 1.5$ and pointed out that the transition angles were off by approximately 9% from the theoretical detachment condition values. The discrepancy between observed and theoretical transition angles was lower for low M_S and became appreciable at higher M_S, which is attributed to increased transmission for stronger incident shocks.

It is understood from the above literature that, unlike the shock reflection phenomenon, which has rich and intensive analytical, computational and experimental documentation, the shock refraction phenomenon has not been investigated rigorously other than those in a few isolated studies, especially in multiphase interfaces. The experimental investigation of shock refraction at gas–liquid interfaces presents significant challenges primarily due to complexities in experimental set-up and constraints associated with high-speed imaging of the multiphase phenomena. This paper discusses a systematic study of the shock refraction phenomenon in an air–water interface, theoretically defending the experimentally observed transition criteria. We also present RRR and BPR patterns, hitherto unobserved experimentally. We conclude with a complete map of the refraction patterns, including all incident shock regimes, supported by shock polar analysis. The experimental and computational set-up are discussed in § 2, followed by the discussion of various shock refraction patterns in § 3. We consolidate with a map of different shock refraction patterns in M_S-complementary wedge angle plane.

2. Methodology

2.1. *Experimental set-up: vertical shock-tube*

A compression-driven closed-ended tiltable vertical shock tube has been designed and fabricated to create a planar shock. It is specifically designed to have an oblique air–water interface so that shock impinges at the interface at a predetermined angle. The Vertical Shock Tube (VST) facility at the Ballistics and High-Speed Flow Lab at IIT, Madras is shown in figure 1 along with the schematic. It is a square shock tube with a cross-section of 90 mm $\times$ 90 mm. The shock tube consists of two main parts: the driver and the driven sections, separated by a scored plastic diaphragm of thickness 400 μm. The driver section is 0.6 m long with a high-pressure (HP) inlet on the top, while the driven section is 2.4 m long, with an inlet and drain for the liquid (water) at the bottom (see figure 1). A 25.4-mm-thick quartz glass window of 70 mm $\times$ 300 mm is used to provide optical

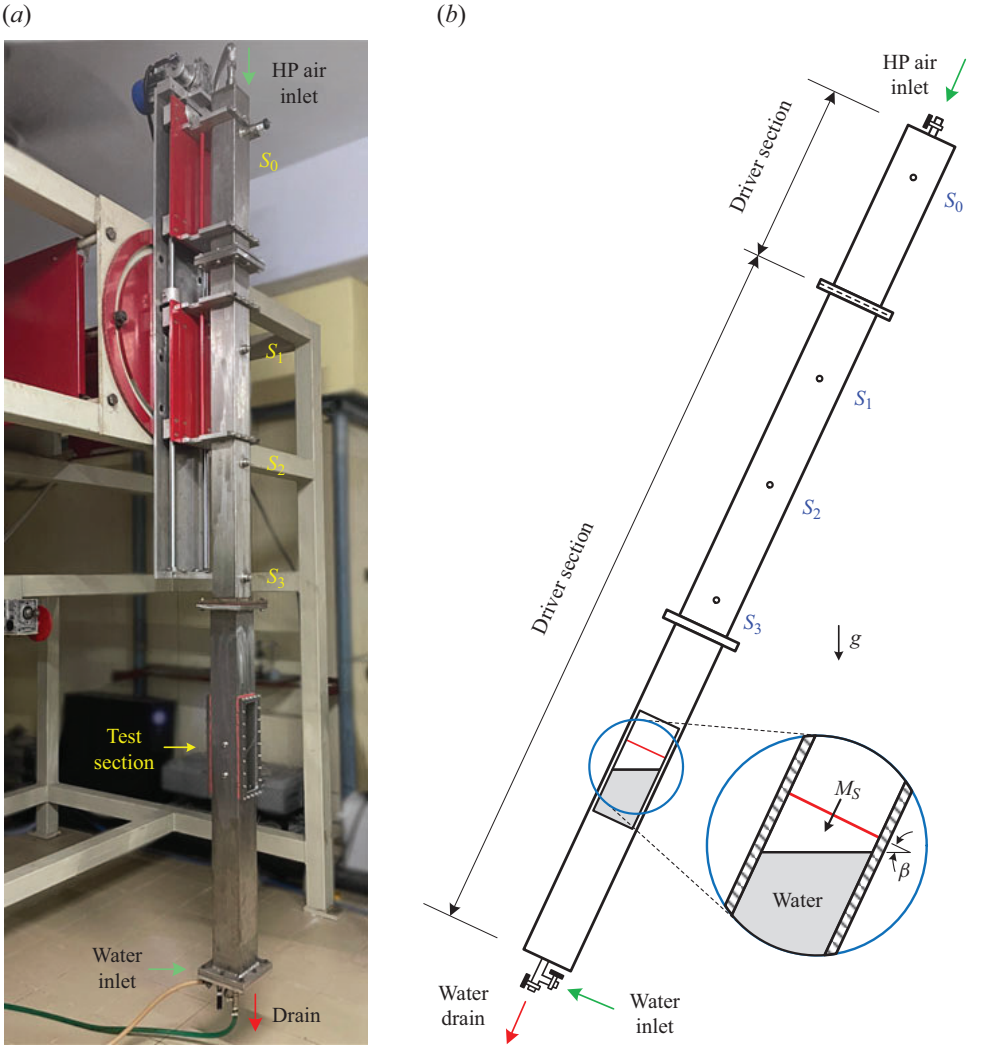

Figure 1. (*a*) The VST facility at the Ballistics and High-speed Flow lab in IIT Madras. (*b*) Schematic diagram of the VST. The solid red lines indicate the incident shock with Mach number M_S.

access for schlieren visualisation towards the end of the driven section. A Z-type schlieren set-up is used for the visualisation with a Cavilux smart laser (640 nm) with a minimum pulse width of 10 ns and an IX-726 high-speed camera, with a maximum frame rate of 1×10^6 f.p.s. and a minimum exposure time of 293 ns. The experiments have been carried out in the bulb-setting mode of the camera with an exposure time of 1 μs and 10 ns for the laser pulses. The strobing frequency is set to 30 kHz, corresponding to 30 000 f.p.s. for the camera. The entire shock tube is 3 m long and is designed for a maximum shock Mach number of 2.4 using air as the operating gas.

The shock tube contains pressure ports, marked S_0 to S_3. The driver pressure is measured from S_0 using ASPT-11u, a piezo-resistive sensor with a sampling frequency of 2 kHz. The diaphragm rupture pressure ratio is calculated from the maximum driver pressure recorded up to the diaphragm rupture. The driven section is maintained at atmospheric conditions, and it has three PCB-113B26 series dynamic pressure sensors located at S_1, S_2 and S_3,

separated by 400 mm from each other. The incident shock Mach number M_S (indicated by the red solid line in figure 1*b*) is evaluated from these sensor readings. All PCB sensors have a maximum sampling frequency of up to 500 kHz.

The shock tube is mounted on a rail to allow for vertical (up and down) motion and is actuated by a motor and pulley system. This allows easy access to the diaphragm section to change the diaphragm after each experiment. It also has a stepper motor that permits the rotation of the entire shock tube about the axis perpendicular to the plane of the shock tube. A maximum tilting angle of up to 65° can be achieved in the current set-up with an accuracy of 0.1°. After placing the diaphragm between the driver and the driven section, the shock tube is rotated to the desired angle, measured by a digital inclinometer. Water at room temperature (300 K) is fed slowly through the bottom inlet until it reaches the required height to be visible in the test-section window. The generated shock wave is always perpendicular to the axis of the shock tube, while the air–water interface remains horizontal due to gravity. Therefore, the inclination angle β between the shock wave and the interface is decided by the angle of rotation of the shock tube axis with respect to the vertical, as shown in figure 1(*b*).

The experiments are carried out at a shock strength, $\zeta \approx 0.43 \pm 0.005$, where

$$\zeta = \frac{p_{pre\text{-}shock}}{p_{post\text{-}shock}} = \left(1 + \frac{2\gamma}{\gamma + 1}(M_S^2 - 1)\right)^{-1}. \tag{2.1}$$

The literature on similar problems (Takayama & Ben-Dor 1989; Nourgaliev *et al.* 2005) identifies this shock strength to be in the weak incident shock regime with a shock Mach number, $M_S = 1.46$. The shock Mach number is measured experimentally using three different approaches: (i) diaphragm rupture pressure ratio (measured from S_0); (ii) pressure sensors in the driven section; (iii) postprocessing the schlieren image and verified to be within the 2 % error margin.

2.2. *Numerical methodology*

A compressible multiphase solver based on the OpenFOAM software framework called BlastFoam is used to simulate the shock refraction phenomenon over an air–water interface (Heylmun, Vonk & Brewer 2022). BlastFoam is a robust solver generally used to simulate explosive detonations and airblasts with high accuracy, as it has higher-order numerical method implementations, various equation of state models, including the stiffened gas equation of state and precise interface capturing techniques.

The current study uses the finite volume method with a second-order accurate Harten, Lax and van Leer contact approximate Riemann solver, based on the work of Toro, Spruce & Speares (1994) for flux evaluation and an explicit strong stability preserving four-stage fourth-order Runge–Kutta method (Spiteri & Ruuth 2002) with adjustable time stepping, for temporal discretisation. The gradients are calculated using the least square discretisation scheme and van Leer flux limiters (van Leer 1974). The volume of fluids method is used to capture the interface. The volume fraction (α) is a bound value ranging from 0 to 1, and typically, $\alpha_i = 0.5$ is considered to be the interface between the two fluids. The following sections discuss the details of the models and governing equations.

2.2.1. *Modelling of water: stiffened gas equation*

Over the years, water has been modelled using different equations of states, such as Tait's equation (Dymond & Malhotra 1988) and the stiffened gas equation (Le Métayer, Massoni

& Saurel 2004). In this study, the stiffened gas equation is used to model water. Solids and liquids can be assumed as ideal gases with a specific ratio of heat capacities, γ, after a particular stiffening pressure characterised by the constant p_∞. The stiffened gas equation of state and its thermodynamic property relations are given by Harlow & Amsden (1968) as

$$p(\rho, e) = \rho(\gamma - 1)(e - e_{ref}) - \gamma p_\infty, \tag{2.2}$$

$$e(\rho, T) = c_v T + \frac{p_\infty}{\rho} + e_{ref}, \tag{2.3}$$

$$s(p, T) = c_v \ln \frac{T^\gamma}{(p + p_\infty)^{\gamma - 1}} + s_{ref}, \tag{2.4}$$

where p, ρ, T, e, e_{ref}, s, s_{ref} and c_v are the pressure, density, temperature, specific internal energy, reference specific internal energy, specific entropy and reference specific entropy and specific heat capacity at constant volume, respectively. Substituting (2.3) into (2.2) yields the thermal equation of state as

$$p(\rho, T) = \rho(\gamma - 1)c_v T - p_\infty. \tag{2.5}$$

The thermodynamic relations between the specific heat capacities at constant pressure (c_p), constant volume (c_v), the gas constant ($R = c_p - c_v$) and the ratio of specific heats ($\gamma = c_p/c_v$) of the gas still holds. It should be noted that the ideal gas equation of state is recovered if $p_\infty = 0$. The speed of sound in a stiffened gas is given by the following modified equation:

$$a = \sqrt{\frac{\gamma(p + p_\infty)}{\rho}}. \tag{2.6}$$

Following Yeom & Chang (2013) for water, $\gamma = 2.8$ and $p_\infty = 850$ MPa is used in the current study. This combination, along with $c_v = 1495$ J (kg K)$^{-1}$, maintains the physical properties of water, such as density ($\rho = 1053$ kg m^{-3}), specific heat capacity ($c_p = 4186$ J (kg K)$^{-1}$) and speed of sound ($a = 1503$ m s^{-1}) at standard atmospheric conditions.

2.2.2. *Governing equations*

The basic governing equation of the multifluid BlastFoam solver is that of the five-equation model (Zheng *et al.* 2011) given as

$$\partial_t \boldsymbol{U} + \boldsymbol{\nabla} \cdot \boldsymbol{F} = \boldsymbol{S}, \tag{2.7}$$

where $\boldsymbol{U}$, $\boldsymbol{F}$ and $\boldsymbol{S}$ are the vectors of the conservative variables, fluxes and source terms, respectively, defined as

$$\boldsymbol{U} = \begin{pmatrix} \alpha_1 \\ \alpha_1\rho_1 \\ \alpha_2\rho 2 \\ \rho \boldsymbol{u} \\ \rho E \end{pmatrix}, \quad \boldsymbol{F} = \begin{pmatrix} \alpha_1 \boldsymbol{u} \\ \alpha_1\rho_1 \boldsymbol{u} \\ \alpha_2\rho_2 \boldsymbol{u} \\ \rho \boldsymbol{u} \otimes \boldsymbol{u} + p\boldsymbol{I} \\ (\rho E + p)\boldsymbol{u} \end{pmatrix}, \quad \boldsymbol{S} = \begin{pmatrix} \alpha_1 \boldsymbol{\nabla} \cdot \boldsymbol{u} \\ 0 \\ 0 \\ 0 \\ 0 \end{pmatrix}. \tag{2.8a–c}$$

In the above definitions, $\boldsymbol{u}$, ρ and E are the mixture velocity, density and total energy. The individual phase density and volume fraction are ρ_i and α_i, respectively, where subscript i

Fluid	γ	p_∞ (Pa)	ρ (kg m^{-3})	c_p (J (kg K)$^{-1}$)	c_v (J (kg K)$^{-1}$)	M_W (g mol^{-1})
Air	1.4	0	1.176	1005	718	28.97
Water	2.8	8.5×10^8	1053	4186	1495	3.09

Table 1. Gas constants used in the numerical simulation.

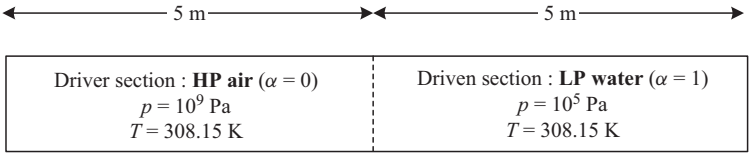

Figure 2. Schematic of the air–water shock tube test case.

represents fluid 1 or 2. It has mass conservation equations for each phase and a transport equation for the volume fraction. Pressure is defined using the respective equations of state. As there are only two phases involved in the current problem, volume fraction and mixture density are defined as follows:

$$\alpha_1 + \alpha_2 = 1, \tag{2.9}$$

$$\rho = \alpha_1 \rho_1 + \alpha_2 \rho_2, \tag{2.10}$$

$$p_i = (\gamma_i - 1)\rho_i e_i - \gamma_i a_i. \tag{2.11}$$

In this study, air is modelled as an ideal gas, while water is modelled as a stiffened gas. Equation (2.11) represents the equation of state in the Mie–Grüneisen form (Zheng *et al.* 2011), where γ_i is the specific heat ratio, and a_i is the reference pressure (p_∞). e_i is the specific internal energy of the fluid defined as

$$e_i = c_v T + \frac{a_i}{\rho}. \tag{2.12}$$

The gas constant values used in modelling air and water are tabulated in table 1. Inviscid simulations are carried out by setting viscosity (μ) to zero.

2.2.3. *Solver validation: air–water shock tube test case*

A one-dimensional, two-fluid (air–water) shock tube test case from Liou *et al.* (2008) is simulated using the BlastFoam solver. The shock tube is 10 m in length, as shown in figure 2. The driver is initialised to high-pressure air, and the driven section is initialised to low-pressure water. The initial pressure ratio between the driver and driven section is 10^4. The gas constants mentioned in the previous section are used to model air and water. As time progresses, a strong shock travels inside the water to the right and expansion waves travel left into the air. The results are extracted at $t = 2.5$ ms for three different grid systems of 200, 500 and 1000 grid points, respectively. Figure 3 shows the comparison of pressure and volume fraction in comparison with the exact analytical solution. As the grid is refined, the shock and interface locations become more defined and follow the exact solution accurately.

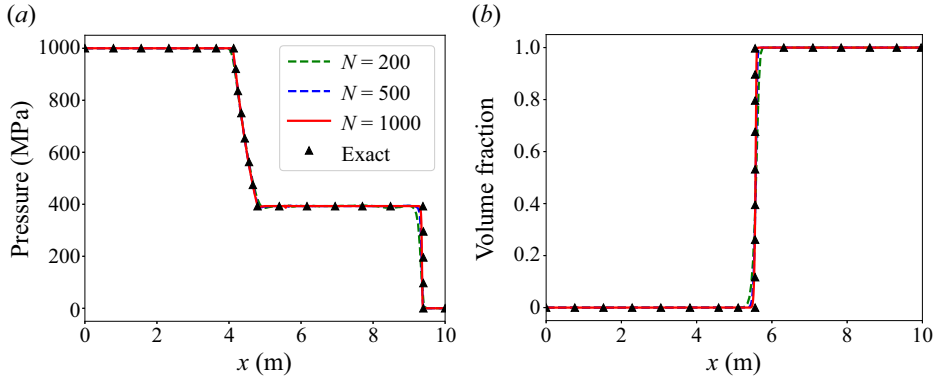

Figure 3. Air–water shock tube test case results at $t = 2.5$ ms: (*a*) pressure plot; (*b*) volume fraction plot.

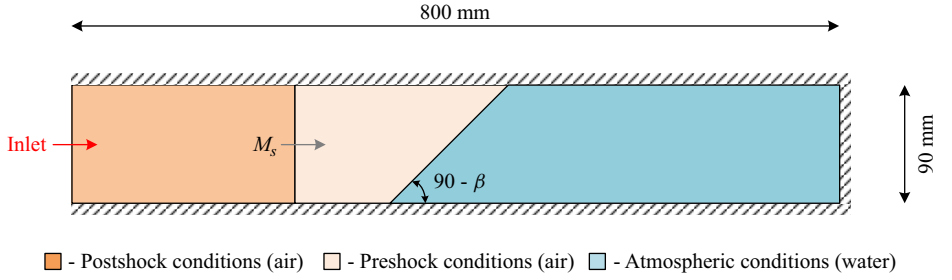

Figure 4. Set-up for the numerical simulation of a shock wave refraction over a water wedge.

	Air		
Flow variables	Postshock conditions	Preshock conditions	Water
α	0	0	1
p (Pa)	235 173.823	101 325	101 325
ρ (kg m^{-3})	2.109	1.17665	1053.018
u (m s^{-1})	224.236	0	0

Table 2. The initial conditions used to simulate a moving shock of strength $\zeta = 0.43$.

2.2.4. *Numerical domain*

Simulating the entire 3-m-long two-dimensional (2-D) shock tube with air and water can be computationally expensive. Hence, a reduced 2-D rectangular domain is considered wherein simulations are set up such that the incident shock wave is initially at a fixed distance from the inclined interface and carried out until the shock reaches the end of the interface. The numerical domain is a rectangle consisting of three regions, as shown in figure 4. The shock wave is initialised in air, with post and preshock conditions mentioned in table 2, such that it travels towards the right. Water is initialised to be on the right-hand side of the domain with the required inclination angle at atmospheric temperature and pressure. The shock wave induces a flow velocity from left to right as it moves, and hence, the left-hand face of the domain is set to be an inlet boundary with the postshock conditions. All the other boundaries are set as inviscid walls. The domain is discretised evenly using a structured cartesian grid ($\delta x = \delta y = 0.25$ mm). The inclined interface

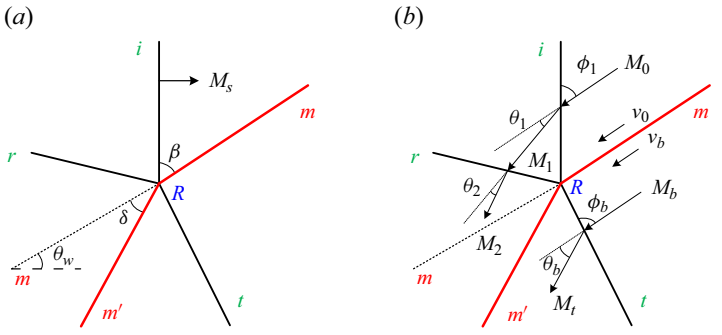

Figure 5. Wave schematics of an RRR in (*a*) the laboratory frame of reference and (*b*) the shock stationary frame of reference: *m*–*m*, undeflected interface; *m*–*m*′, deflected interface; *i*, incident shock; *r*, reflected shock; *t*, transmitted shock; *R*, refraction point.

in a Cartesian grid is not aligned with the cells, resulting in a sawtooth-shaped rough interface. This roughness effect is minimised by considering finer grids. Surface tension and viscosity effects come into the picture only at later time scales where the RMI develops (Carlès & Popinet 2002). In experiments, surface tension results in the development of a liquid meniscus at the walls of the shock tube. The shock refraction pattern is analysed over the interface away from the walls, where the interface inclination remains constant. Therefore, surface tension, along with gravity, is neglected in the simulations.

3. Results and discussion

The following section presents experimental and numerical results for a shock Mach number $M_S = 1.46$, along with the shock polar diagrams to justify the observed shock refraction patterns at the interface. To draw these shock polars, the analytical shock relations for a stiffened gas are required. Although the stiffened gas equation of state has been used widely to model liquids, shock relations have not been specifically derived. Therefore, the isentropic relations and explicit closed-form Rankine–Hugoniot jump conditions are derived (refer to Appendix A for the analytical relations).

3.1. *Refraction with transmitted shock*

From the existing knowledge of shock refraction at a slow–fast interface, for a small inclination angle (β), the observed refraction pattern should comprise of three shocks, all intersecting on the interface at a single point. This type of refraction pattern is known as RRR. Although the existence of an RRR for the air–water system is known from previous works, it should be noted that the exact 2-D refraction pattern has not been verified or visualised experimentally until now.

Figure 5(*a*) is a schematic representation of a typical regular shock refraction pattern at an interface in the laboratory frame of reference. In this case, the incident shock wave *i* reflects from and transmits into the second medium as *r* and *t* shocks, respectively, at the refraction point *R* on the interface, in addition to deflecting the shocked interface (*mm*′). The interface is inclined at an angle $\beta = 90^\circ - \theta_w$, where the wedge angle, θ_w, is the angle between the interface and the horizontal.

Assuming all waves to be planar and travelling at a constant velocity, these refracting systems can be transformed from the pseudosteady laboratory frame of reference to a

shock-stationary frame of reference (shown in figure 5*b*) using the following equation:

$$M_0 = \frac{M_S}{\sin(90 - \theta_w)}. \tag{3.1}$$

The shock stationary frame of reference is with respect to the refraction point R on the interface for regular refraction. In (3.1), M_0 is the incoming flow Mach number in the transformed frame of reference. To maintain an undisturbed interface upstream of the shock, the incoming flow velocity in the second medium should be equal to the flow velocity along the interface in the first medium (Henderson 1966), i.e.

$$v_b = v_0. \tag{3.2}$$

Therefore, the incident flow Mach number in the second medium (M_b) can be obtained as a function of M_0 and the speed of sound of the two media (see (3.3)). It is calculated by using the stiffened gas parameters mentioned in table 1 in the following equations:

$$M_b = M_0 \left(\frac{a_0}{a_b}\right), \tag{3.3}$$

$$M_b = M_0 \sqrt{\left(\frac{\gamma_0}{\gamma_b}\right)\left(\frac{M_{W,b}}{M_{W,0}}\right)}. \tag{3.4}$$

Figure 6 shows the experimental schlieren images (on the top of the panel) and numerical pressure gradient contours (bottom of panel images, which are mirror images about the horizontal axis) of an incident shock wave ($M_S = 1.46$), refracting from an air–water interface at $\beta = 15^\circ$ corresponding to $\theta_w = 75^\circ$, at various time instances. The shock wave moves from left-hand side (air) to the right-hand side (water). The first time instant at which the shock wave enters the experiment window is taken to be the reference time, $t = 0$ s. The schlieren images are processed to find the initial shock distance from the interface. This shock stand-off distance is given as the location of the shock in the simulations to obtain time-resolved numerical pressure gradient contours. The images clearly show that the numerical simulation matches accurately with the experiment (figure 6*a*,*b*). At a later time, shown in figure 6(*c*), the incident shock i reflects back as a shock wave r, forming a reflection pattern that resembles an RR in air. Also, it transmits a shock wave t, into water that travels along the interface attached to the refraction point R. Figure 6(*c*) also clearly shows the corner-generated wave (a curved brighter wave) from the leading edge of the wedge, trailing just behind the transmitted shock. This interaction is responsible for the curvature of the transmitted shock towards the bottom wall of the shock tube. The incident shock looks thin in the experimental schlieren images due to the difficulty in positioning the knife edge to obtain proper intensity variations in air and water simultaneously.

The shock polar diagram is constructed to gain further insight into this shock refraction pattern. From figure 5, it can be seen that for an RRR, the shock angle ϕ_1 is the same as the inclination angle of the interface β. With the M_0 and ϕ_1 as known variables, the incident polar (i-polar) can be drawn using (A15) and the θ–ϕ–M relation (see (A17)). Similarly, using the Mach number behind the incident shock M_1, the reflected polar (r-polar) can be drawn with θ_1, the transformed deflection angle for the incident shock, as the anchor point on the i-polar. The transmitted polar (t-polar) is drawn using (A15), also at $\theta = 0^\circ$, as the flow velocity is along the interface. The solution point is the intersection of all three polars, and the deflection angle at this point corresponds to the deflection angle of the interface.

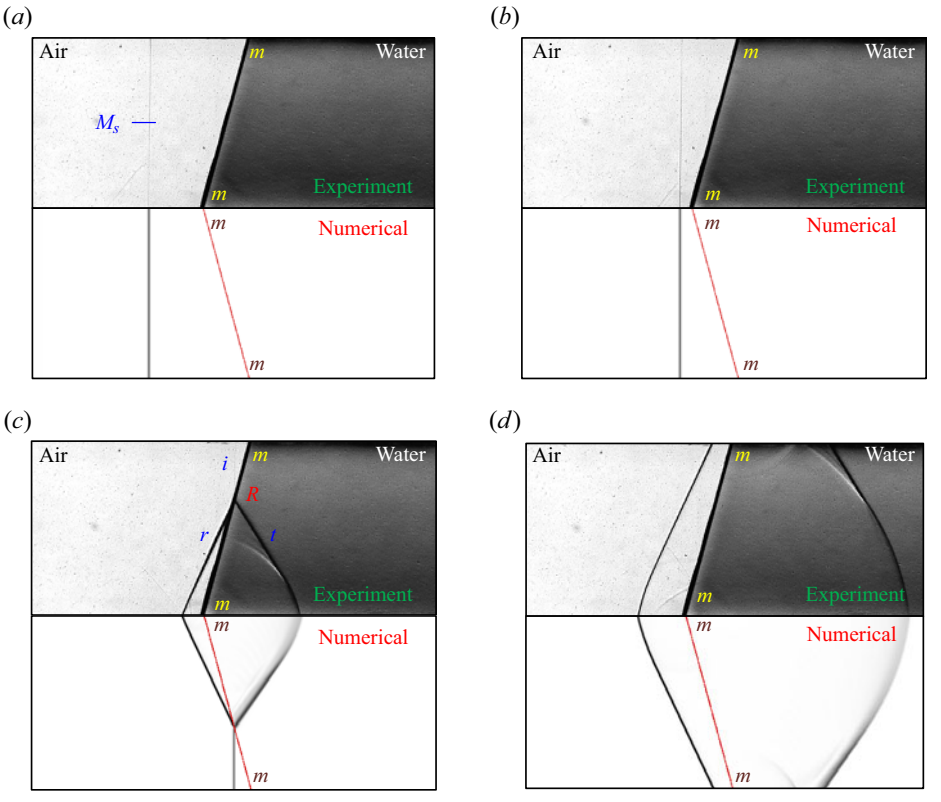

Figure 6. Combined images of experiment and numerical simulation of an incident shock ($M_S = 1.46$) refracting over water interface ($\beta = 15^\circ$) at various time instances producing an RRR: m–m, interface; i, incident shock; r, reflected shock; t, transmitted shock; R, refraction point. Here (*a*) $t = 66$ µs, (*b*) $t = 100$ µs, (*c*) $t = 133.33$ µs, (*d*) $t = 166.66$ µs.

The shock polar for $\beta = 15^\circ$ is drawn in figure 7. In the transformed frame of reference, with respect to the reflection point R, the i, r-polars correspond to the flow Mach numbers of 5.6 and 4.81, respectively, whereas the t-polar is drawn for a flow Mach number $M_b = 1.3$ in water, obtained from (3.4). The pressure jump caused by a normal shock in water is orders of magnitude higher than that in air, and hence the t-polar is much larger compared with the i-, r-polars. Therefore, it appears to be a vertical line on smaller scales of p/p_0 (green line in figure 7). The region of interest is enlarged in the inset in figure 7, where the solution is given by the intersection of the transmitted polar and the weak part of the reflected polar, indicated with a yellow marker. The deflection angle at the solution point is the interface deflection angle behind the shock wave. From the shock polar solution in figure 7, it can be seen that for the present case of $\beta = 15^\circ$, the interface deflection angle is approximately 0.005°. For a given shock Mach number, 3.1 and 3.4 indicate that M_b is inversely proportional to β. Therefore, any β less than 15° also produces an RRR. On the other hand, as β increases, M_b becomes progressively less supersonic. This leads to the flattening of the transmitted polar. Hence, the RRR solution point shifts rightward along the r-polar and upwards along the weak part of the t-polar. Consequently, the interface deflection angle (δ) and the transmitted shock angle (ϕ_b) increase with an increase in β. This clarifies the forward-leaning nature of the transmitted wave (increasing ϕ_b) in an RRR until it becomes normal to the interface at a critical inclination angle, where it transitions

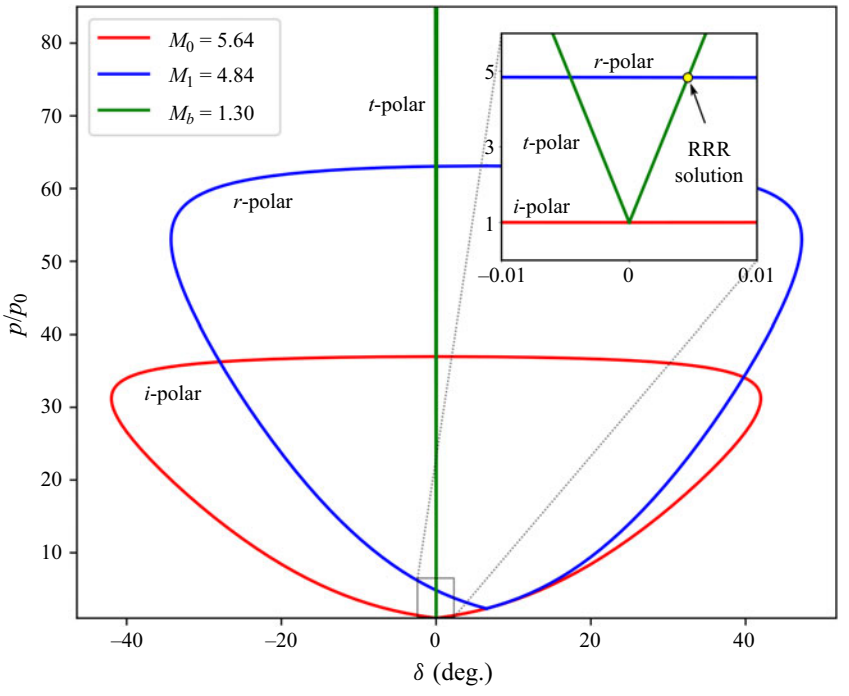

Figure 7. Shock polar solution of an RRR: $M_S = 1.46$; $\beta = 15^\circ$.

into the next refraction pattern in the sequence. Nourgaliev *et al.* (2005) also reported this phenomenon in their numerical simulations. By virtue of the variation in the energy being reflected owing to the transmission of the wave into water, Wan *et al.* (2017) noted that the reflected shock structure in a water wedge is not quite equivalent to that in a solid wedge. Therefore, the above discussion leads to two observations of interest;

(i) an RRR solution exists until a critical inclination angle is reached, after which the *t*-polar becomes too small to intersect with the *r*-polar;
(ii) in water wedges, although the interface deflection angles (δ) are negligible, the reflections from a solid wedge and water wedge are not directly comparable, as the energies of the transmitted waves into the second medium are different in each case.

3.2. *Bound precursor refraction*

Beyond the critical inclination angle discussed above, the corner-generated wave inside water catches up to the refraction point and alters the curvature of the already weak transmitted shock as shown in figure 8(*a*). Therefore, the shock refraction pattern obtained immediately after the critical inclination angle is identified as the BPR. Bound precursor refraction is characterised by a regular reflection in the slow medium (air) and a curved transmitted shock in the fast medium (water), and all shocks intersect at the refraction point *R* on the interface. Figure 8(*b*) shows the BPR pattern obtained in the experiment and numerical simulation for an inclination angle of 19.7°. (The accuracy of the VST facility is only 0.1° and the inclination angle of 19.7° is the closest we could get to the BPR transition point. Theoretically, this angle should correspond to an RRR with a transmitted shock angle, $\phi_b = 90 - \epsilon$, where ϵ is a very small angle. The analytical transmitted shock

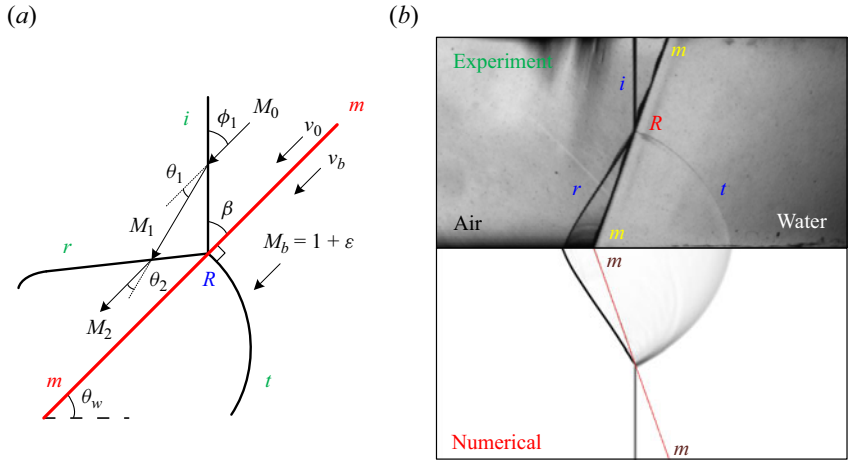

Figure 8. (*a*) Schematic of a BPR in the shock stationary frame of reference. (*b*) Comparison of experimental schlieren image and numerical pressure gradient contours of a BPR: $M_S = 1.46$; $\beta = 19.7^\circ$. Here *m*–*m*, interface; *i*, incident shock; *r*, reflected shock; *t*, transmitted shock; *R*, refraction point.

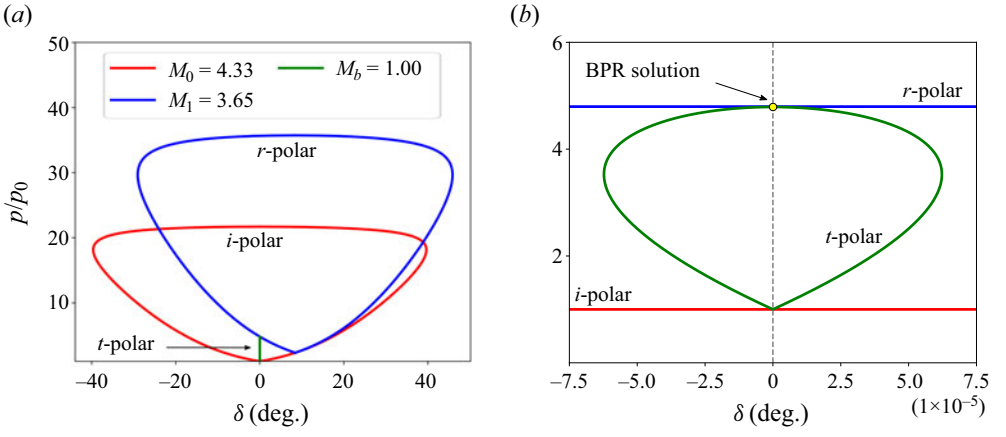

Figure 9. The RRR → BPR transition point. (*a*) The shock polar solution: $M_S = 1.46$; $\beta = 19.7148^\circ$. (*b*) Enlarged view showing the intersection point of *r*-, *t*-polars.

angle (ϕ_b) for an inclination angle of 19.7° is calculated to be 89.995°.) It is seen that the transmitted wave is near normal at the refraction point, travelling at the same speed as that of the incident shock along the interface. Therefore, a crucial difference between an RRR and a BPR is the nature of the transmitted shock structure inside water.

From a shock polar perspective, the transition from RRR → BPR occurs at a point of tangency between the *r*-polar and the *t*-polar. It should also be noted that M_b is only slightly supersonic $(1 + \varepsilon)$ in BPR. In gas–gas interfaces, the RRR → BPR transition is defined as the tangency condition between the reflected and the transmitted polars at a particular positive deflection angle ($\delta > 0$) while the transmitted wave is at some shock angle ($\phi_b \neq 90^\circ$) to the interface. In the present case of an air–water interface, the transmitted polar is so small in comparison with the reflected polar, and the tangency condition hence occurs almost close to the normal shock point of the *t*-polar as shown in figure 9. The BPR domain exists up to an inclination angle where M_b becomes sonic. It is identified that the inclination angles for the transition RRR → BPR and the sonic

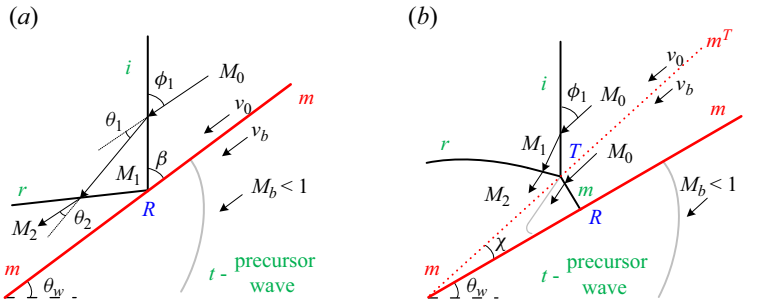

Figure 10. Wave schematics of precursor refractions in shock stationary frame of reference: (*a*) FPR; (*b*) free precursor Mach refraction (FMR). Here *m*–*m*, interface; *i*, incident shock; *r*, reflected shock; *m*, Mach stem; *t*, transmitted shock; *R*, refraction point.

condition of M_b lie very close to each other for a given shock Mach number. Hence, the BPR domain extends only for a very small range of β ($\approx 0.0001^\circ$), where the transmitted polar is no longer tangent to the reflected polar. Therefore, for practical considerations of air–water interfaces, BPR can be considered a transition pattern rather than a separate refraction pattern, unlike that of gas–gas interfaces.

3.3. *Free precursor refractions*

Increasing the inclination angle further, beyond the BPR domain, results in free precursor refractions, where there is no transmitted shock ($M_b < 1$) but rather a transmitted pressure wave travelling ahead of the refraction point. In this domain, M_b remains subsonic, decreasing further with an increase in β. Figure 10 shows the schematic (shock stationary frame of reference) of the two different types of refractions possible in this domain: free precursor refractions with RR and MR in air, respectively.

After the BPR transition point, for the same shock strength, with the increase in inclination angle, it can be seen that the incident shock reflects as an RR in air with a weak transmitted curved pressure wave, previously referred to as 'spherical' transmitted shock (Takayama & Ben-Dor 1989), in water. This *t*-wave travels at the speed of sound of water and is much faster than the shock speed. Therefore, it detaches itself free from the refraction point *R* and travels ahead. Hence, the refraction pattern shown in figure 10(*a*) that includes an RR in air and the precursor *t*-wave is termed as an FPR. An inclination angle (β) of 30° corresponds to such a condition, and the refraction patterns obtained in the experiment and numerical simulation are shown in figure 11. Nourgaliev *et al.* explained that this precursor wave is evanescent in nature and that very little back transmission was observed. From the present experimental schlieren images, it is verified that there is no significant back-transmission of the precursor wave into air. Therefore, the reflection pattern in air is not affected by the presence of a transmitted forerunning pressure wave. The shock polar solution of an FPR at $\beta = 30^\circ$ inclination is also drawn in figure 11. The solution consists only of the reflection in air, given by the RR solution point, as there is no *t*-polar owing to the subsonic nature of the transformation-induced flow Mach number inside water.

Upon further increase in inclination angle (β), M_b becomes increasingly subsonic, with a difference that the reflection pattern (in air) transitions from regular to MR as shown in figure 10(*b*). In Nourgaliev *et al.* (2005), the above refraction pattern was identified as an FNR. An FNR is characterised by an MR modified by the back-transmitted precursor shock wave and the presence of centred expansion waves generated from the foot of the

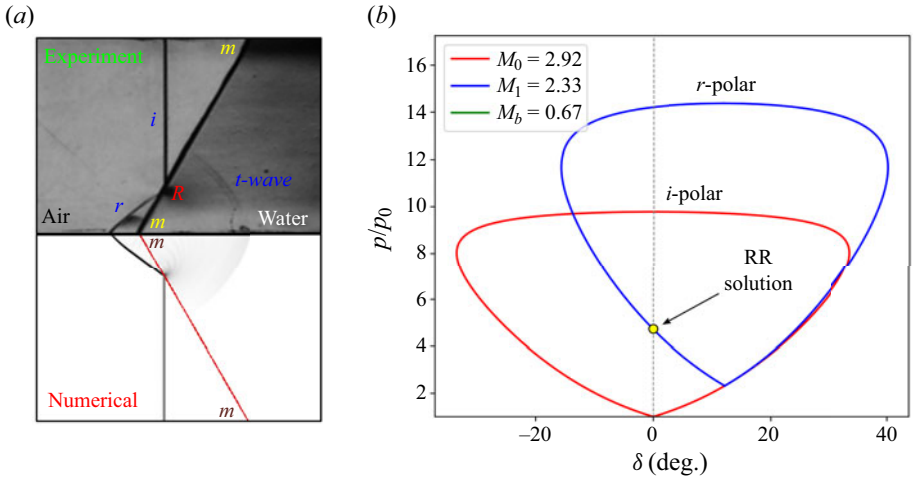

Figure 11. Free precursor refraction with a regular reflection at $M_S = 1.46$, $\beta = 30^\circ$ and its shock polar solution.

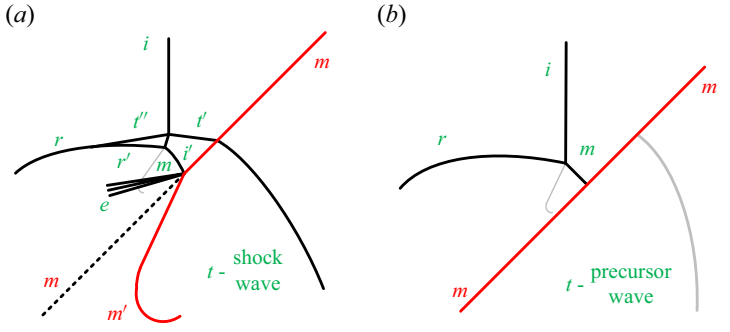

Figure 12. Schematic wave diagrams of (*a*) FNR; (*b*) FMR. Here $m{-}m$, initial interface; $m{-}m'$, deformed interface; *i*, incident shock; *r*, reflected shock; *e*, expansion waves; *m*, Mach stem; *t*, transmitted shock/wave; t', back-transmitted *t* shock/pressure wave; t', modified t'; i', modified incident shock; r', modified reflected shock.

Mach stem in the lighter medium as shown in figure 12(*a*). Also, an FNR deflects the interface to a finite angle. FNR is a complex wave system comprising nine waves, whereas the current refraction pattern comprises only four waves as the evanescent precursor wave does not back-transmit into air. Despite being similar, these are two very different shock systems. Henceforth, this refraction system will be referred to as an FMR. The differences between an FNR and an FMR can be understood from the comparative schematic diagrams shown in figure 12.

For an FMR, the transformation from the pseudosteady laboratory frame of reference to the shock stationary frame of reference is with respect to the triple point T and not the refraction point R. Therefore, in the transformed frame of reference, the apparent interface (mm^T) is aligned parallel to the triple-point trajectory and inclined at an angle equal to $90^\circ - \theta_w^c$, where θ_w^c is the sum of θ_w and the triple point trajectory angle χ (see figure 10*b*). It should be noted that for an FMR, in (3.1), θ_w^c should be used to calculate the incoming flow Mach number M_0 in the transformed frame of reference instead of θ_w. Also, for an

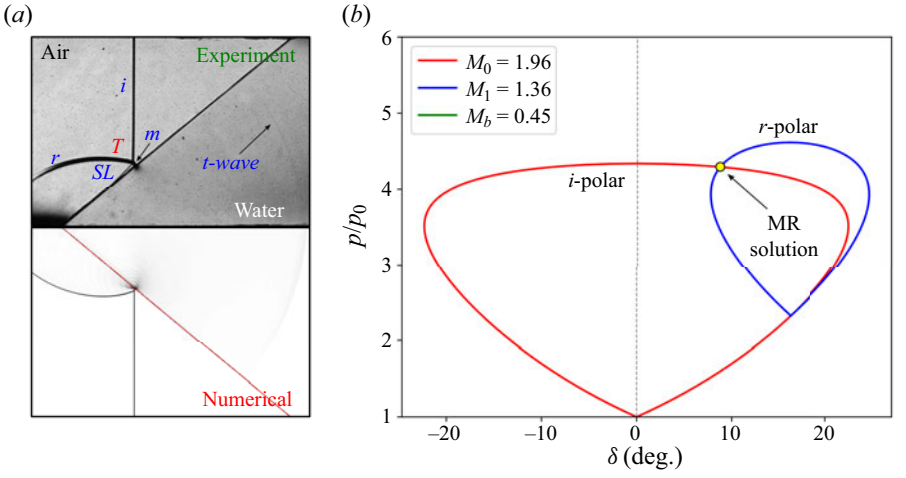

Figure 13. Free precursor Mach refraction: $M_S = 1.46$; $\beta = 50^\circ$.

RRR and FPR, the shock angle ϕ_1 is the same as the inclination angle of the interface β, while it is equal to $90 - \theta_w^c$ for an FMR.

Figure 13 shows the experimental and numerical images of an FMR obtained at $\beta = 50^\circ$. A small Mach stem and a slip line (*SL*) are clearly visible, along with the presence of a transmitted precursor wave (*t-wave*), confirming a FMR. The shock polar solution for such a reflection is given by the intersection of the *r*-polar with the *i*-polar. It should be noted that the shock polar solution drawn in figure 13 corresponds to the apparent interface inclination angle $(90 - \theta_w^c)$. The triple point trajectory χ is measured from the experimental schlieren image to be $\approx 2^\circ \pm 0.1^\circ$. The FMR domain includes all irregular reflection patterns possible in air, such as double Mach reflection (DMR), transitional Mach reflection, von Neumann reflection, single Mach reflection and weak shock reflections (Vasilev reflection, Guderley reflection) (Ben-Dor 2007) with a free precursor wave in water.

Wan *et al.* investigated the first and second triple point trajectories of DMR cases for a shock Mach number of 4 in both solid and water wedges and reported them to be linear. Therefore, the irregular reflections from a water wedge were proved to be self-similar. However, no comment was made on the self-similar nature of the transmitted wave and, by extension, the refraction pattern as a whole. Figure 14(*a*) shows the numerical contours of an FMR occurring at $M_S = 2.2$ and $\beta = 50^\circ$. In the figure, the triple point trajectory, highlighted as a dashed green line, is found to be linear, once again confirming the self-similar nature of the reflection pattern. Figure 14(*b*) shows the distance travelled by the transmitted free precursor wave inside water along the bottom wall (marked S_t in figure 14*a*) as a function of time. The pixel error for these measurements is 0.11 mm pixel^{-1}. The linearity of the plot verifies that the refraction pattern as a whole is self-similar. Also, the slope of this line gives the velocity of the transmitted precursor wave as 1503 m s^{-1}, the speed of sound of water.

In the shock stationary frame of reference with respect to the triple point, for a given shock Mach number, another critical inclination angle exists beyond which the flow behind the incident shock M_1 becomes subsonic. In reflections over solid wedges, various combinations of (M_S, θ_w^c) that correspond to this particular reflection type fall into the no reflection domain (NRD) (Vasilev, Elperin & Ben-Dor 2008). It should be noted that this domain exists only in the (M_S,θ_w^c)-plane. In the physical (M_S,θ_w)-plane, these reflections

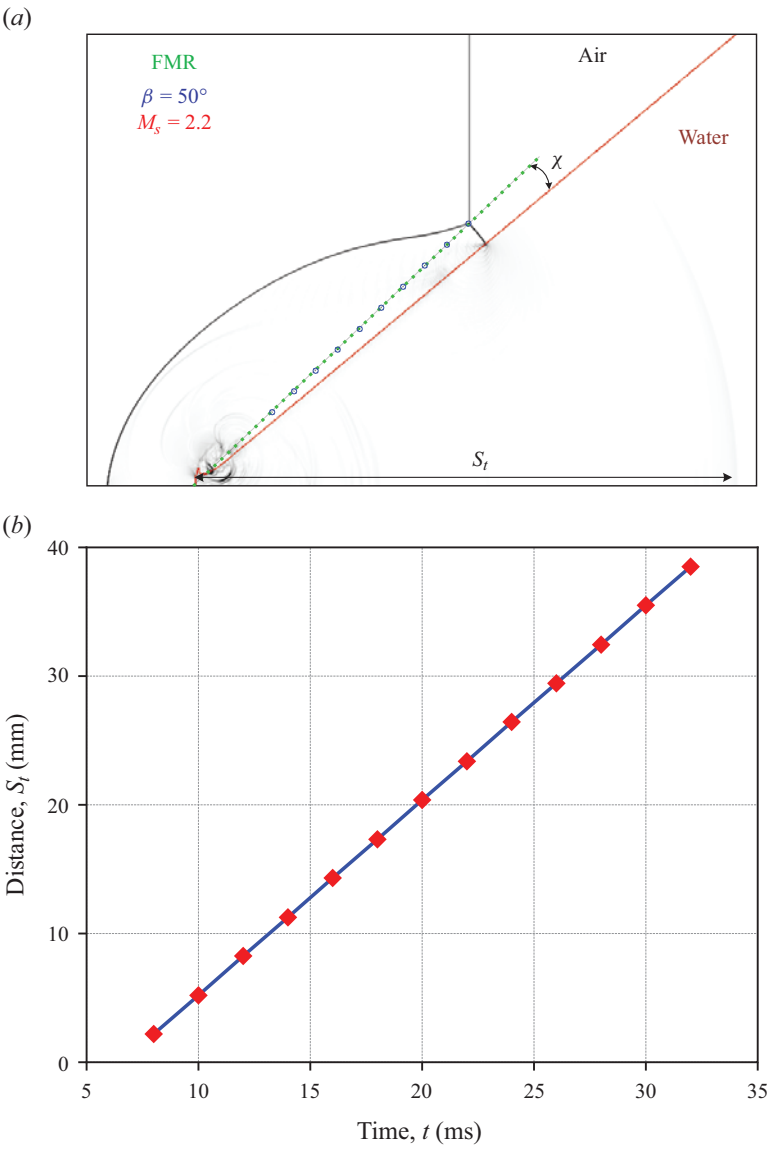

Figure 14. Self-similar nature of the irregular refraction (FMR) over an air–water interface at an inclination angle $\beta = 50^\circ$ and a shock Mach number $M_S = 2.2$. (*a*) The triple point trajectory (χ). (*b*) The distance travelled by the transmitted precursor wave (S_t) inside water along the bottom wall at various time instances.

mostly correspond to single Mach reflections (Ben-Dor 2007), and so for the air–water refraction system, they fall into the FMR category.

3.4. *Refraction sequence*

The refraction sequence for $M_S = 1.46$ is identified from experiments and numerical simulations as RRR → FPR → FMR, with BPR being a transition pattern from RRR to FPR. Figure 15 shows the numerical pressure gradient contours for various cases considered in the order of increasing angle of inclination, including head-on impingement

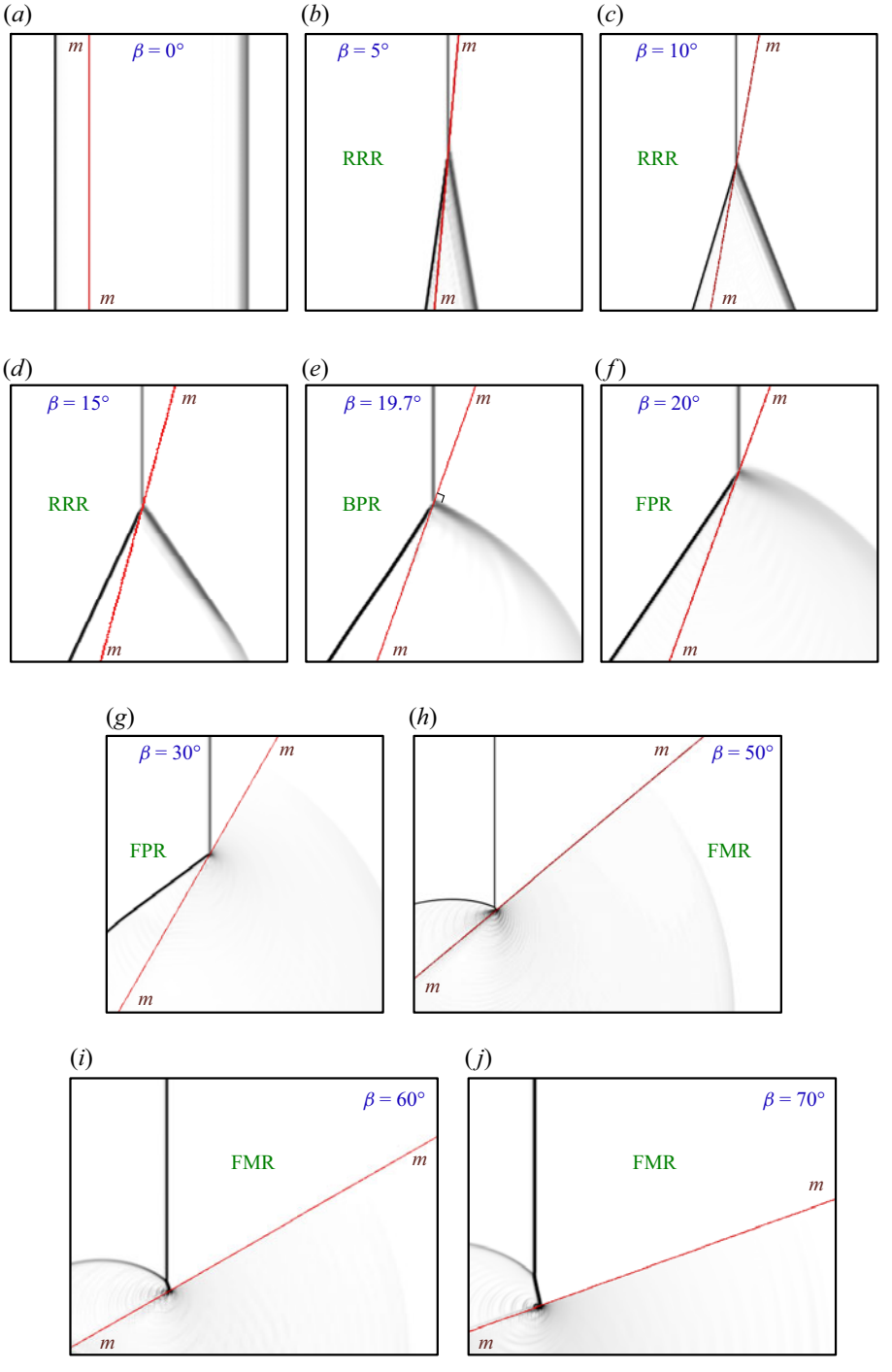

Figure 15. Numerical pressure gradient contours of shock refraction at an air–water (air on the left-hand side and water on the right-hand side) interface for $M_S = 1.46$ exhibiting (*a*) shock transmission for head-on impingement; (*b–d*) RRR; (*e*) BPR; (*f,g*) FPR; (*h–j*) FMR – the red line ($\alpha = 0.5$) indicates the interface.

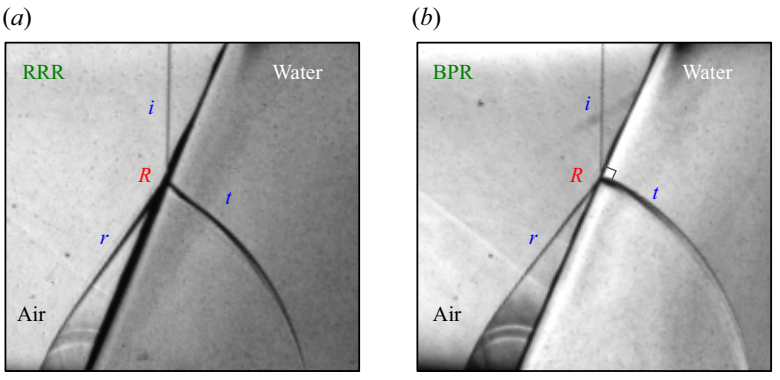

Figure 16. Refraction patterns obtained at a higher shock Mach number in the very weak incident shock regime: i, incident shock; r, reflected shock; t, transmitted shock; R, refraction point. Here (a) RRR, $M_S = 1.7$, $\beta = 22.2°$; (b) BPR, $M_S = 1.7$, $\beta = 23.1°$.

($\beta = 0°$). In addition to $M_S = 1.46$, experiments and numerical simulations are done for higher shock Mach numbers within the very weak incident shock regime. Experiments are carried out for $M_S = 1.7$. The critical angle at which the BPR transition pattern occurs is calculated to be 23.13° from the analytical transition criterion. Figure 16 shows the refraction patterns obtained at two different inclination angles. At an inclination angle of 22.2°, figure 16(a) clearly shows the presence of a transmitted oblique shock inside water attached to the refraction point R, indicating that the refraction pattern is an RRR. Whereas at 23.1°, it can be seen that a BPR occurs, as shown in figure 16(b). Numerical simulations for a higher shock Mach number of 2.2 are performed to reinforce the results further. The refraction patterns obtained for various interface inclination angles are shown in figure 17. Bound precursor refraction occurs at $\beta = 30.56°$ as predicted by the analytical transition criterion ($M_b = 1$). Also, the refraction sequence is still RRR $\rightarrow$ (BPR) $\rightarrow$ FPR $\rightarrow$ FMR.

3.5. *Transition lines*

With the help of the understanding from shock polars, it is now possible to draw the transition lines from one refraction pattern to another. From § 3.2, it is understood that an RRR transforms into BPR when the reflected polar becomes tangent to the transmitted polar at the normal shock conditions. Therefore, for a given M_S, it reduces to solving a set of nine equations: (3.1), (3.3), Mach number, θ–ϕ–M and pressure ratio relations for the incident, reflected and transmitted shocks, along with the following conditions to get the inclination angle corresponding to RRR $\rightarrow$ BPR transition:

$$\theta_1 - \theta_2 = 0, \tag{3.5}$$

$$\left(\frac{p_2}{p_1}\right)\left(\frac{p_1}{p_0}\right) = \left(\frac{p_b}{p_t}\right)_{NS}. \tag{3.6}$$

In the numerical study of Nourgaliev *et al.* (2005) (referred to as N2005), for a shock strength of $\zeta = 0.426$ ($M_S = 1.467$), BPR was predicted to occur at $\beta = 37.5°$. The present experimental schlieren image in figure 8(b) confirms that this transition pattern occurs at a much lower inclination angle of $\beta = 19.7°$. The overprediction BPR transition in N2005 must be from the improper modelling of the physical properties of water as discussed below.

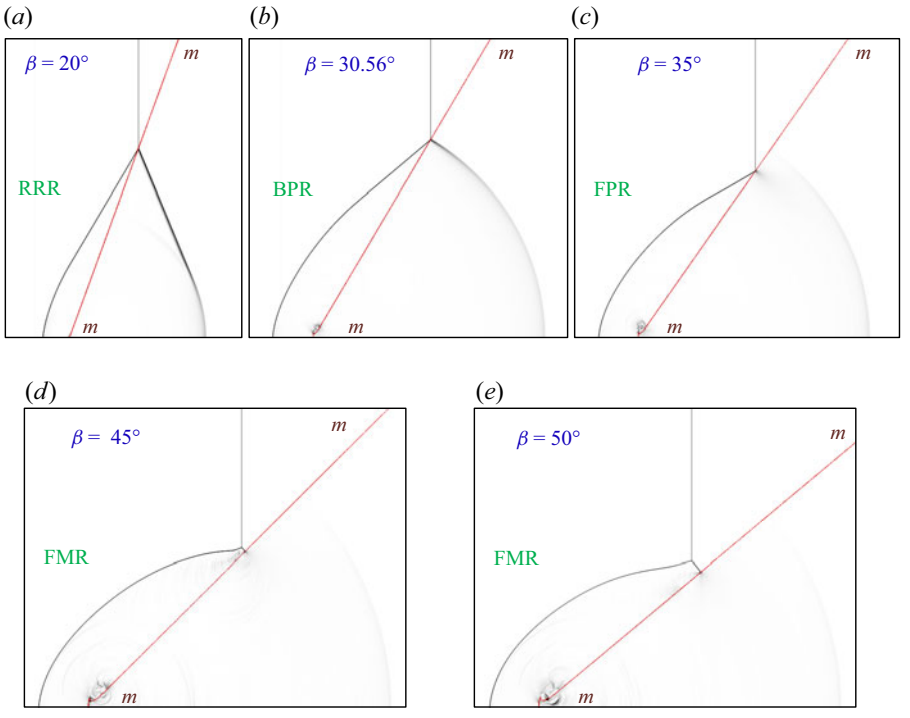

Figure 17. Numerical pressure gradient contours of shock refraction at an air–water (air on the left-hand side and water on the right-hand side) interface for $M_S = 2.2$ exhibiting (*a*) RRR; (*b*) BPR; (*c*) FPR; (*d*,*e*) FMR – the red line ($\alpha = 0.5$) indicates the interface.

The stiffened gas parameters used by N2005 are $\gamma = 2.8, p_\infty = 3.036 \times 10^8$ Pa, while the current study uses $\gamma = 2.8, p_\infty = 8.5 \times 10^8$ Pa (Yeom & Chang 2013) to model water at low pressures. The combination of (γ, p_∞) and initial conditions of N2005 give the following physical properties of water as a stiffened gas: specific heat capacity $c_p = 1297.6$ J (mol K)$^{-1}$; speed of sound $a_b = 902.89$ m s^{-1}; molecular weight $M_{W_b} = 9.967$ g mol^{-1}. The (γ, p_∞) combination used in the current study gives the following physical properties of water as a stiffened gas: specific heat capacity $c_p = 4186$ J (mol K)$^{-1}$; speed of sound $a_b = 1503.5$ m s^{-1}; molecular weight $M_{W_b} = 3.09$ g mol^{-1}. It should be noted that the speed of sound of water in N2005 is much less than the actual value of 1500 m s^{-1}.

To verify if the overpredicted BPR transition angle in N2005 is from the incorrect modelling of water, the authors performed numerical simulations by modelling water with both sets of stiffened gas parameters of water mentioned above. These numerical simulations are carried out for the shock Mach number 1.467 and an inclination angle of 37.5°. Figure 18(*a*) shows the numerical pressure gradient contours using N2005 parameters and figure 18(*b*) using Yeom & Chang (2013). The prediction of N2005 is reproduced and shows BPR in figure 18(*a*), whereas using the realistic values of the stiffened gas parameter predicts FPR.

To get the BPR → FPR transition line, M_b is set to 1 in (3.3) and is solved for β. In the precursor refraction domain, it is established that there is no significant back-transmission to alter the reflection pattern. Therefore, FPR → FMR transition is given by the detachment criterion (θ_D). For the NRD line, the following equation, given

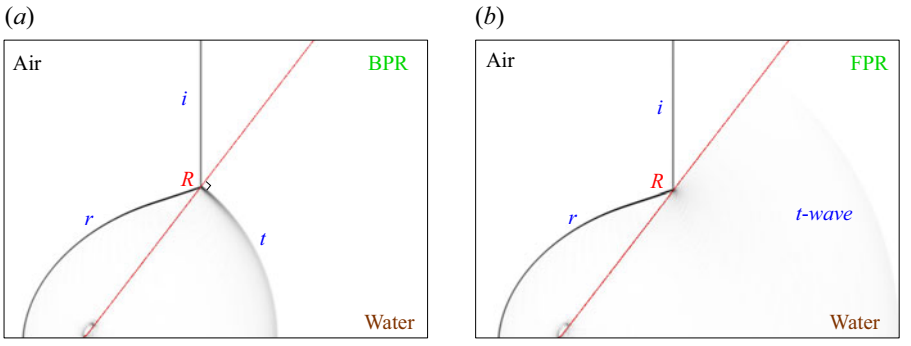

Figure 18. Refraction patterns obtained for an $M_S = 1.46$ and $\beta = 37.5^\circ$ using (*a*) the stiffened gas parameter used in N2005 and (*b*) the current study's stiffened gas parameter. The prediction of N2005 is reproduced and shows BPR in (*a*), whereas using the realistic values of the parameter from Yeom & Chang (2013) predicts FPR as in (*b*). Here (*a*) $P_\infty = 3.036 \times 10^8$ Pa for BPR; (*b*) $P_\infty = 8.5 \times 10^8$ Pa for FPR.

by Vasilev *et al.* (2008), is used:

$$\sin^2\phi = \frac{1}{2\gamma_0 M_0^2}\left\{\frac{1}{2}(\gamma_0 - 3) + \frac{1}{2}(\gamma_0 + 1)M_0^2 + (\gamma_0 + 1)^{1/2} \times \left[\frac{1}{4}(\gamma_0 + 9) + \frac{1}{2}(\gamma_0 - 3)M_0^2 + \frac{1}{4}(\gamma_0 + 1)M_0^4\right]^{1/2}\right\}. \tag{3.7}$$

Based on the above discussion, the transition lines separating various shock refraction domains in an air–water system are drawn in figure 19. It is evident that there are three different regimes based on refraction pattern sequences: very weak; weak; and strong shock regimes. When the shock Mach number increases (in the weak incident shock regime), it accommodates larger inclination angles until a free precursor refraction can occur. Hence, it is possible for an MR to occur in air along with a transmitted shock in water, giving rise to an IRMR. Wan *et al.* (2017) has reported observing such refraction patterns for shock Mach numbers 3 and 4 at $\theta_w = 45^\circ$. Therefore, with the absence of FPR in the weak shock regime, RRR transitions directly into an IRMR. Upon further increase in β, IRMR transitions into an FMR through a bound precursor refraction with a Mach reflection. On the other hand, the shock Mach numbers of the strong shock regime are large enough to eliminate free precursor refraction altogether. This regime has a transmitted shock wave at all inclination angles, and the only possible refraction patterns are RRR and IRMR. Table 3 presents the refraction sequences identified for the three shock strength regimes and their ranges.

3.6. *Comparison of numerical simulations with previous experimental studies in the very weak incident shock regime*

3.6.1. *Experiments by Takayama & Ben-Dor (1989)*

Takayama & Ben-Dor studied the shock wave reflections off a water wedge for a wide range of shock Mach numbers ($1.06 < M_S < 2.35$). From figure 19, it is clear that these shock Mach numbers fall under the very weak incident shock regime. They reported a weak transmitted spherical 'shock' wave inside water, centred exactly at the beginning of the interface in all their experimental cases. From the present study, it is now understood

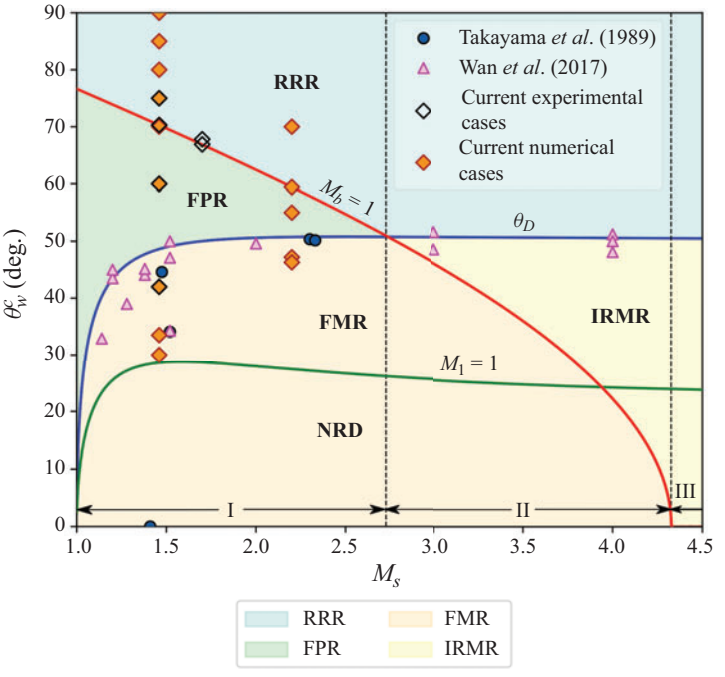

Figure 19. Shock strength regimes and transition lines for various shock refraction patterns in (M_S, θ_w^c) plane for air–water (s/f) interface: FPR, free precursor refraction with a regular reflection; FMR, free precursor Mach refraction; IRMR, irregular refraction with a MR; I, very weak shock regime; II, weak shock regime; III, strong shock regime.

Regime	M_S range	Refraction sequence with increasing β
Very weak shock	$1 < M_S < 2.725$	RRR → FPR → FMR
Weak shock	$2.725 < M_S < 4.325$	RRR → IRMR → FMR
Strong shock	$M_S > 4.325$	RRR → IRMR

Table 3. Refraction sequences of a shock wave over an air–water interface in various shock strength regimes.

that they observed the transmitted spherical precursor wave, as all their cases lie in the FPR domain in the (M_S, θ_w^c)-plane, and that the RR → MR transition they had investigated was actually FPR → FMR transition. To elucidate their results, numerical simulations are carried out. For a shock Mach number of 1.47 and wedge angle of 44.3° ($\beta = 45.7°$), Takayama & Ben-Dor reported an RR (FPR) as shown in figure 20. The wedge angle corresponding to the detachment criteria for this shock Mach number is 48.7°, indicating that the reflection should be an MR. From the numerical pressure gradient contours in the inset of figure 20, it is seen that the reflection in air is indeed an MR with a very small Mach stem ($\chi \approx 0.3°$). A smaller domain 80 mm × 40 mm mesh of $\delta x = \delta y = 0.025$ mm is used to resolve such fine details. It seems that the experiments carried out by Takayama & Ben-Dor failed to capture the small Mach stem in the FMR due to poor frame resolution, leading them to conclude the reflection as an RR. The shock polar analysis confirms an FMR for the said (M_S, θ_w) combination. The experimental interferogram photographs of three other cases ($M_S = 1.52$, $\theta_w = 26.5°$), ($M_S = 2.3$, $\theta_w = 46.7°$) and ($M_S = 2.33$, $\theta_w = 50°$) with a relatively stronger incident shocks reported by Takayama & Ben-Dor, also belong to the FMR configuration: single Mach reflection with a free precursor, CMR

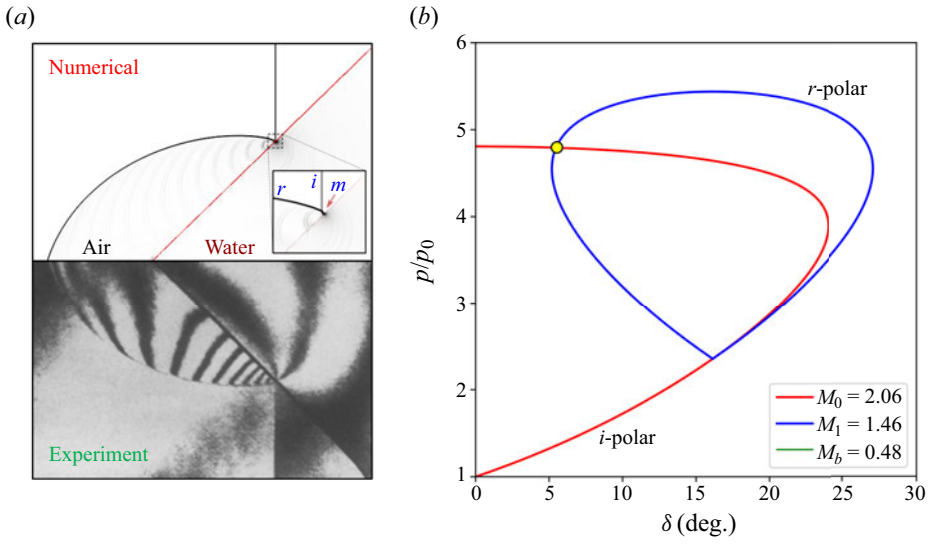

Figure 20. Comparison of the Takayama & Ben-Dor (1989) under-resolved experiment and OpenFOAM simulation showing FMR along with shock polar solution for $M_S = 1.47$, $\beta = 45.7°$ ($\theta_w = 44.3°$).

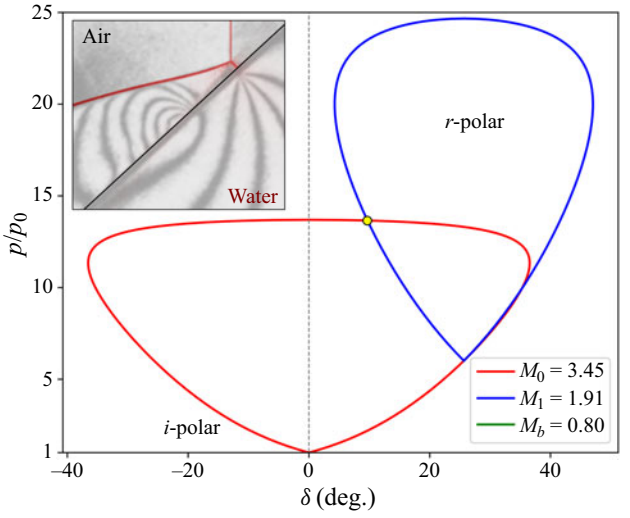

Figure 21. Shock polar solution and comparison of the Takayama & Ben-Dor (1989) experimental interferogram photograph of a complex Mach reflection (CMR) with OpenFOAM simulation (superimposed) showing FMR for $M_S = 2.3$, $\beta = 43.3°$ ($\theta_w = 46.7°$).

(from the new-state-of-knowledge (Li & Ben-Dor 1995), this corresponds to a transitional Mach reflection, evident from the presence of a kink and supersonic flow behind the incident shock wave in the lab frame of reference.) with a free precursor and DMR with a free precursor respectively. To demonstrate the correctness and the reproducibility of the numerical simulations and the shock polars, a comparison of the FMR pattern obtained for an (M_S, θ_w) combination of (2.3, 46.7°) is shown in figure 21.

3.6.2. *Experiments by Wan et al. (2017)*

Most recently, Wan *et al.* (2017) performed experiments and numerical simulations of a shock wave refracting over water wedges. To the best knowledge of the authors, this is the

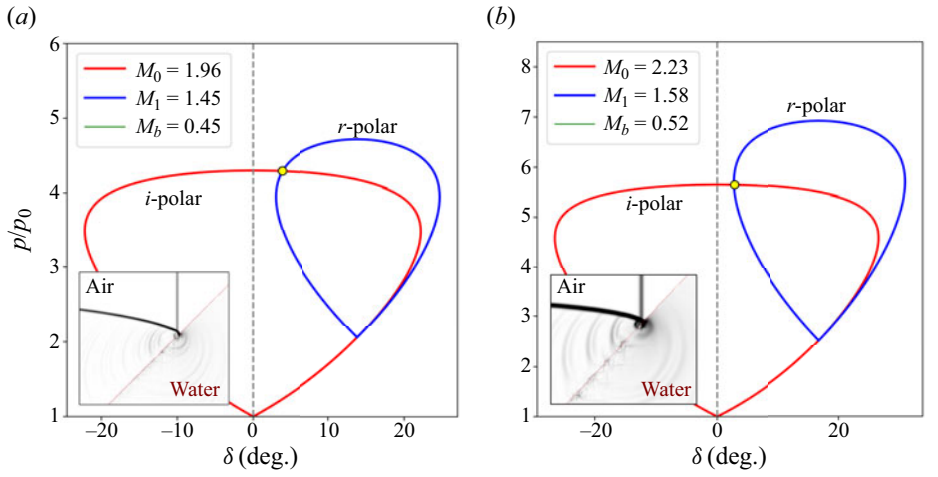

Figure 22. Shock polar solution and the numerical contours of FMR cases identified to be FPR by Wan *et al.* (2017): (*a*) $M_S = 1.38$, $\beta = 45^\circ$ ($\theta_w = 45^\circ$); (*b*) $M_S = 1.52$, $\beta = 43^\circ$ ($\theta_w = 47^\circ$).

only other experimental work that has been conducted with respect to 2-D planar shock refraction over oblique air–water interfaces. They conducted experiments for several shock Mach numbers in the very weak incident shock regime, namely, 1.2, 1.38 and 1.52. The RR $\rightarrow$ MR transition angles over water wedges were identified and compared with the solid wedges and the detachment criterion. For five cases in the very weak shock regime, experimental schlieren images were reported: $M_S = 1.38$, $\beta = 45^\circ, 47^\circ$ and $M_S = 1.52$, $\beta = 40^\circ, 43^\circ, 65^\circ$. Cases 1, 3 and 4 were identified as RR, while cases 2 and 5, with higher β value, were identified as MR, which are equivalent to FPR and FMR from the perspective of refraction patterns. It should be noted that in the work of Wan *et al.*, the primary focus was on the reflections above the water and no attempts were made to classify the observed refraction patterns.

OpenFOAM simulations are carried out in a rectangular domain (60 mm $\times$ 38.1 mm) with 25 μm grid size for all five cases. The shock polar analysis of 45° and 43° inclination for shock Mach numbers 1.38 and 1.52 (cases 1 and 4) both correspond to an FMR with $\chi = 0.15^\circ$ and $\chi = 0.1^\circ$. The numerical pressure gradient contours of these cases shown in figure 22 confirm the presence of an MR in air. As explained earlier, the sawtooth nature of the interface generates the 'ripple waves' on either side of the interface. As numerical contour plots the pressure gradient magnitude, the slip line cannot be seen in MR. The authors suspect that these MRs were not resolved in their experiments because the Mach stem heights of these FMR configurations are too small to be captured over the finite apparent thickness of the interface due to insufficient resolution. Furthermore, as the incident shock moves over the interface, the Mach stem height growth is also very small. The minuscule nature of this MR can be understood better from the contour image in figure 22 when the incident shock is almost at the top end of the water wedge where the Mach stem is approximately three cells tall. The reasons mentioned above could explain the underpredicted RR(FPR) $\rightarrow$ MR(FMR) transition angles from the experiments. They also ran high-resolution simulations for $M_S = 4$, $\theta_w = 40^\circ, 50^\circ$ and reported numerical schlieren images corresponding to IRMR and RRR. They are consistent with refraction patterns expected at $M_S = 4$ in the weak incident shock regime from figure 19.

4. Conclusion

This study employs experiments and numerical simulations to investigate the phenomenon of pseudosteady refraction of a 2-D planar moving shock wave when it interacts with an inclined air–water interface. To analyse the refraction patterns analytically, shock and isentropic flow relations are derived for a stiffened gas to generate shock polars in water. Two refractions previously reported from numerical simulations, namely, RRR and BPR, are observed experimentally for the first time. Two different types of free precursor refractions are also observed in the present study: one with a regular reflection (FPR) and one with a Mach reflection (FMR). These cases are numerically verified using OpenFOAM simulations.

The overpredicted transition point from RRR $\rightarrow$ FPR in the previous work due to the improper modelling of water properties has been corrected in the present work with verifications from experiments, numerical results and shock polars. Furthermore, the shock structures of an FMR were initially thought to be the same as that of an FNR. The need for a separate refraction pattern is ascribed by highlighting the key differences between the two. Transition criteria from one refraction pattern to another are obtained and are used to draw the transition lines in an (M_S, θ_w^c)-plane. Three regimes are identified based on the refraction pattern sequence as very weak, weak and strong incident shock regimes. In the weak and strong regimes, the refraction sequences are predicted to be RRR $\rightarrow$ IRMR $\rightarrow$ FMR and RRR $\rightarrow$ IRMR, respectively, which was not reported previously. Experimental results from the prior literature on shock reflections off a water wedge in the very weak incident shock regime are compiled and classified into various refraction patterns in their respective shock strength regimes. It is also observed that the reason for under-predicted experimental RR(FPR) $\rightarrow$ MR(FMR) transition points in earlier experimental studies is the minuscule value of the triple point trajectory angle, which is practically challenging to visualise in shock tubes with a smaller width.

Declaration of interests. The authors report no conflict of interest.

Author ORCIDs.
C. Anbu Serene Raj https://orcid.org/0009-0001-4773-2650;
S. Vishnu Prasad https://orcid.org/0009-0009-7295-6160;
G. Rajesh https://orcid.org/0000-0002-4459-7676;
A. Sameen https://orcid.org/0000-0001-7113-4952.

Appendix A. Shock relations for a stiffened gas

A.1. *Isentropic relations*

For any thermodynamic process from state 1 to state 2 in water, from (2.4), change in entropy (Δs) can be written as

$$s_2 - s_1 = c_v \ln \frac{T_2^\gamma}{(p_2 + p_\infty)^{\gamma-1}} - c_v \ln \frac{T_1^\gamma}{(p_1 + p_\infty)^{\gamma-1}}. \tag{A1}$$

For $\Delta s = 0$, the above equation with some rearrangement can be recast to obtain the pressure ratio relation as

$$\frac{p_2}{p_1} = \left(1 + \frac{p_\infty}{p_1}\right)\left(\frac{T_2}{T_1}\right)^{\gamma/(\gamma-1)} - \frac{p_\infty}{p_1}. \tag{A2}$$

From the stiffened gas equation of state (2.5), it can be seen that $(p+p_\infty)/\rho T = (\gamma - 1)c_v$ is constant. Hence, the density ratio for an isentropic process is obtained to be

$$\frac{\rho_2}{\rho_1} = \left(\frac{T_2}{T_1}\right)^{1/(\gamma-1)}. \tag{A3}$$

Therefore, the isentropic relations for stiffened gas can be summarised as

$$\frac{T_2}{T_1} = \left(\frac{p_2+p_\infty}{p_1+p_\infty}\right)^{(\gamma-1)/\gamma} = \left(\frac{\rho_2}{\rho_1}\right)^{\gamma-1}. \tag{A4}$$

A.2. *Normal-shock relations*

The one-dimensional adiabatic equations for the flow across the normal shock are given by the continuity, momentum and energy equations as

$$\rho_1 u_1 = \rho_2 u_2, \tag{A5}$$

$$p_1 + \rho_1 {u_1}^2 = p_2 + \rho_2 {u_2}^2, \tag{A6}$$

$$h_1 + \frac{{u_1}^2}{2} = h_2 + \frac{{u_2}^2}{2}, \tag{A7}$$

where ρ, u, p and h denote the density, velocity, pressure and enthalpy. The alternate energy equation derived by substituting the stiffened gas equation of state is the same as that of an ideal gas. Therefore, the relation of the characteristic Mach number M^* to the flow Mach number is

$$M^{*2} = \frac{(\gamma+1)M^2}{2+(\gamma-1)M^2}. \tag{A8}$$

The above equation is the same as that of an ideal gas (Liepmann & Roshko 2001). Consequently, the Mach number, density and temperature relations derived using (A9), (A5) and (A7) for a flow across a normal shock wave, remain unchanged for a stiffened gas as follows:

$$M_1^* M_2^* = 1, \tag{A9}$$

$${M_2}^2 = \frac{1+\left(\dfrac{\gamma-1}{2}\right){M_1}^2}{\gamma {M_1}^2 - \left(\dfrac{\gamma-1}{2}\right)}, \tag{A10}$$

$$\frac{\rho_2}{\rho_1} = \frac{u_1}{u_2} = \frac{(\gamma+1){M_1}^2}{2+(\gamma-1){M_1}^2}, \tag{A11}$$

$$\frac{T_2}{T_1} = \frac{T_0/T_1}{T_0/T_2} = \frac{1+\dfrac{\gamma-1}{2}M_1^2}{1+\dfrac{\gamma-1}{2}M_2^2}. \tag{A12}$$

The ratio of pressure, however, is modified by substituting (2.6) in (A6) to be

$$\frac{p_2}{p_1} = 1 + \frac{2\gamma}{\gamma+1}(M_1^2 - 1)\left(1 + \frac{p_\infty}{p_1}\right). \tag{A13}$$

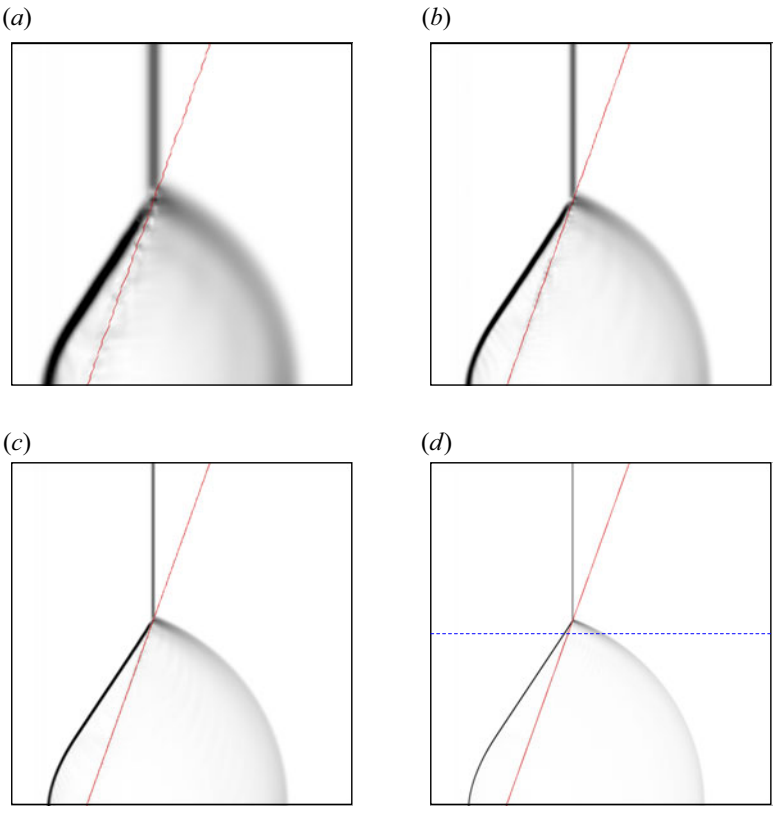

Figure 23. Bound precursor refraction patterns obtained for shock Mach number $M_S = 1.46$ at $\beta = 19.7^\circ$ in different Cartesian meshes. The blue dashed line indicates the y-location at which the data shown in figure 24 is extracted: (*a*) $\delta x = \delta y = 1$ mm; (*b*) $\delta x = \delta y = 0.5$ mm; (*c*) $\delta x = \delta y = 0.25$ mm; (*d*) $\delta x = \delta y = 0.1$ mm.

Hence, (A10), (A11), (A12) and (A13) give the jump conditions across a normal shock wave in a stiffened gas.

A.3. *Oblique-shock relations*

As changes across an oblique shock wave are governed only by the component of velocity normal to the wave, the equations of normal shock are valid for an oblique shock, given that the normal component of the velocity ($M_{n,1}$) is used. Hence, for an oblique shock wave from (A10) and (A12) and (A13), the following relations are used:

$$\frac{\rho_2}{\rho_1} = \frac{u_1}{u_2} = \frac{(\gamma+1){M_{n,1}}^2}{2+(\gamma-1){M_{n,1}}^2}, \tag{A14}$$

$$\frac{p_2}{p_1} = 1 + \frac{2\gamma}{\gamma+1}(M_{n,1}^2 - 1)\left(1 + \frac{p_\infty}{p_1}\right), \tag{A15}$$

$$\frac{T_2}{T_1} = \frac{p_2 + p_\infty}{p_1 + p_\infty}\left(\frac{\rho_1}{\rho_2}\right) = \frac{\left(\dfrac{p_2}{p_1} + \dfrac{p_\infty}{p_1}\right)}{\left(1 + \dfrac{p_\infty}{p_1}\right)\left(\dfrac{\rho_2}{\rho_1}\right)}, \tag{A16}$$

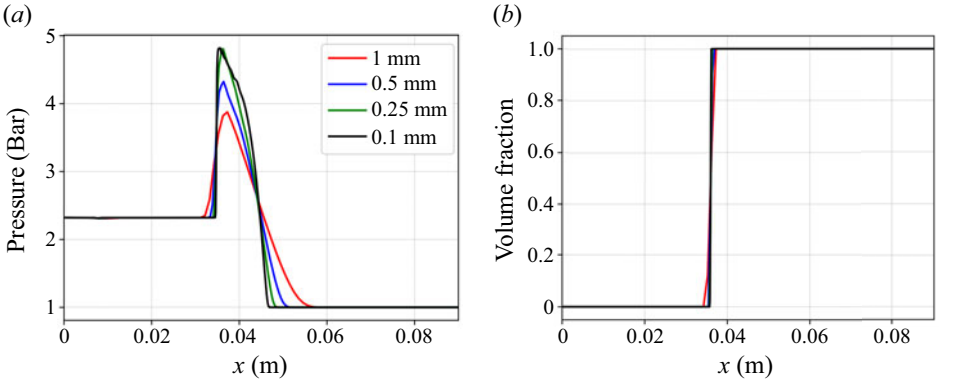

Figure 24. Mesh independency plots for the BPR case: (*a*) pressure plot; (*b*) volume fraction plot.

$$\tan\theta = 2\cot\phi\frac{M_1^2\sin^2\phi - 1}{M_1^2(\gamma + \cos 2\phi) + 2}. \tag{A17}$$

Also, there is no change from ideal gas in the θ–ϕ–M relation as it is derived only from geometric relations and continuity equation.

Appendix B. Mesh independency

The transition patterns and angles can be sensitive to the mesh used. Therefore, a mesh independency study for RRR to FPR transition through BPR is performed for the shock Mach number 1.46. The analytical BPR transition angle for this shock Mach number is 19.715°. Four different meshes of $\delta x = \delta y = 1$ mm, 0.5 mm, 0.25 mm, 0.1 mm are considered for the transition case. Figure 23 shows the resulting pressure contour plots.

From figure 23, it is clear that the shocks are finer as the mesh density increases, whereas, at lower mesh densities, they are smeared. It should be noted that the transition angle is a geometrical parameter in the computational domain for a given shock Mach number. From figure 23, it is clear that all the contour plots give a BPR at the same inclination angle. Hence, the transition angle does not seem to depend on the mesh size. To clarify this further, the pressure and volume fraction variation is extracted along a horizontal line (marked as a dashed blue line in figure 23*d*) located at the centre of this domain ($y = 0.045$ m), just below the refraction point on the interface. Figure 24(*a*) shows that the shock strengths are captured accurately for meshes with a grid spacing of $\delta x = \delta y \leq 0.25$ mm, while figure 24(*b*) shows that except for the mesh with the largest grid spacing ($\delta x = \delta y = 1$ mm), all the other meshes generate a sharp interface. Therefore, for all the simulations in the current study, the 0.25 mm grid is used. Exceptions are those where a finer grid is used to capture the small Mach stems, as explained in § 3.6.

References

ABD-EL-FATTAH, A.M. & HENDERSON, L.F. 1976 Precursor shock waves at a slow-fast gas interface. *J. Fluid Mech.* **76**, 157–176.

ABD-EL-FATTAH, A.M. & HENDERSON, L.F. 1978*a* Shock waves at a fast-slow gas interface. *J. Fluid Mech.* **86** (1), 15–32.

ABD-EL-FATTAH, A.M. & HENDERSON, L.F. 1978*b* Shock waves at a slow-fast gas interface. *J. Fluid Mech.* **89** (1), 79–95.

ARUN KUMAR, R., RAJESH, G. & JAGADEESH, G. 2022 The reflection and refraction of a curved shock front sliding over an air–water interface. *Shock Waves* **32** (6), 497–515.

BEN-DOR, G. 2007 *Shock Wave Reflection Phenomena*, 2nd edn. Springer.

BORISON, A.A., GEL'FAND, B.E., SHERPANEV, S.M. & TIMOFEEV, E.I. 1981 Mechanism for mixture formation behind a shock sliding over a fluid surface. *Combust. Expl. Shock waves* **17** (5), 558–563.

BORISOV, A.A., KOGARKO, S.M. & LYUBIMOV, A.V. 1965 Sliding of detonation and shock waves over liquid surfaces. *Combust. Expl. Shock waves* **1** (4), 19–23.

CARLÈS, P. & POPINET, S. 2002 The effect of viscosity, surface tension and non-linearity on Richtmyer–Meshkov instability. *Eur. J. Mech. (B/Fluids)* **21** (5), 511–526.

DELMONT, P., KEPPENS, R. & VAN DER HOLST, B. 2009 An exact Riemann-solver-based solution for regular shock refraction. *J. Fluid Mech.* **627**, 33–53.

DYMOND, J.H. & MALHOTRA, R. 1988 The Tait equation: 100 years on. *Intl J. Thermophys.* **9** (6), 941–951.

HARLOW, F.H. & AMSDEN, A.A. 1968 Numerical calculation of almost incompressible flow. *J. Comput. Phys.* **3** (1), 80–93.

HENDERSON, L.F. 1966 The refraction of a plane shock wave at a gas interface. *J. Fluid Mech.* **26** (3), 607–637.

HENDERSON, L.F. 1989 On the refraction of shock waves. *J. Fluid Mech.* **198** (1989), 365–386.

HENDERSON, L.F., COLELLA, P. & PUCKETT, E.G. 1991 On the refraction of shock waves at a slow-fast gas interface. *J. Fluid Mech.* **221** (March), 1–27.

HENDERSON, L.F., Jia-Huan, M., Akira, S. & Kazuyoshi, T. 1990 Refraction of a shock wave at an air–water interface. *Fluid Dyn. Res.* **5** (5–6), 337–350.

HENDERSON, L.F., PUCKETT, E.G. & COLELLA, P. 2004 The Anomalous Refraction of Shock Waves in Gases. In *15th Australasian Fluid Mechanics Conference*, vol. 1, pp. 6–8.

HEYLMUN, J., VONK, P. & BREWER, T. 2022 *BlastFoam 6.0 User Guide*. Synthetik Applied Technologies, LLC.

HOSSEINI, H., MOOSAVI-NEJAD, S., AKIYAMA, H. & MENEZES, V. 2014 Shock wave interaction with interfaces between materials having different acoustic impedances. *Appl. Phys. Lett.* **104** (10), 103701.

JAHN, R.G. 1956 The refraction of shock waves at a gaseous interface. *J. Fluid Mech.* **1** (5), 457–489.

KEITH, T.G. & JOHN, J.E. 2006 *Gas Dynamics*. Pearson Education Inc.

LE MÉTAYER, O., MASSONI, J. & SAUREL, R. 2004 Elaborating equations of state of a liquid and its vapor for two-phase flow models. *Intl J. Therm. Sci.* **43** (3), 265–276.

VAN LEER, B. 1974 Towards the ultimate conservative difference scheme. II. Monotonicity and conservation combined in a second-order scheme. *J. Comput. Phys.* **14** (4), 361–370.

LI, H. & BEN-DOR, G. 1995 Reconsideration of pseudo-steady shock wave reflections and the transition criteria between them. *Shock Waves* **5** (1–2), 59–73.

LIEPMANN, H.W. & ROSHKO, A. 2001 *Elements of Gasdynamics*. Courier Corporation.

LIOU, M.S., CHANG, C.H., NGUYEN, L. & THEOFANOUS, T.G. 2008 How to solve compressible multifluid equations: a simple, robust, and accurate method. *AIAA J.* **46** (9), 2345–2356.

LUO, X., DONG, P., SI, T. & ZHAI, Z. 2016 The Richtmyer–Meshkov instability of a 'v' shaped air/SF_6 interface. *J. Fluid Mech.* **802**, 186–202.

MCFARLAND, J., REILLY, D., CREEL, S., MCDONALD, C., FINN, T. & RANJAN, D. 2013 Experimental investigation of the inclined interface Richtmyer–Meshkov instability before and after reshock. *Exp. Fluids* **55** (1), 1640.

MENIKOFF, R. & GROVE, J.W. 1990 Anomalous reflection of a shock wave at a fluid interface. *J. Fluid Mech.* **219**, 313–336.

MESHKOV, E.E. 1969 Instability of the interface of two gases accelerated by a shock wave. *Fluid Dyn.* **4** (5), 101–104.

NOURGALIEV, R.R., SUSHCHIKH, S.Y., DINH, T.N. & THEOFANOUS, T.G. 2005 Shock wave refraction patterns at interfaces. *Intl J. Multiphase Flow* **31** (9), 969–995.

POLACHEK, H. & SEEGER, R.J. 1951 On shock-wave phenomena; refraction of shock waves at a gaseous interface. *Phys. Rev.* **84** (5), 922–929.

RICHTMYER, R.D. 1960 Taylor instability in shock acceleration of compressible fluids. *Commun. Pure Appl. Maths* **13** (2), 297–319.

RODRIGUEZ, V., JOURDAN, G., MARTY, A., ALLOU, A. & PARISSE, J.D. 2016 Planar shock wave sliding over a water layer. *Exp. Fluids* **57** (8), 1–5.

SEMBIAN, S., LIVERTS, M., TILLMARK, N. & APAZIDIS, N. 2016 Plane shock wave interaction with a cylindrical water column. *Phys. Fluids* **28** (5), 056102.

SPITERI, R.J. & RUUTH, S.J. 2002 A new class of optimal high-order strong-stability-preserving time discretization methods. *SIAM J. Numer. Anal.* **40** (2), 469–491.

TAKAYAMA, K. & BEN-DOR, G. 1989 Pseudo-steady oblique shock wave reflections over water wedges. *Exp. Fluids* **8** (3), 129–136.

TORO, E.F., SPRUCE, M. & SPEARES, W. 1994 Restoration of the contact surface in the HLL-Riemann solver. *Shock Waves* **4** (1), 25–34.

VASILEV, E.I., ELPERIN, T. & BEN-DOR, G. 2008 Analytical reconsideration of the von Neumann paradox in the reflection of a shock wave over a wedge. *Phys. Fluids* **20** (4), 046101.

WAN, Q., JEON, H., DEITERDING, R. & ELIASSON, V. 2017 Numerical and experimental investigation of oblique shock wave reflection off a water wedge. *J. Fluid Mech.* **826**, 732–758.

WANG, H., ZHAI, Z. & LUO, X. 2022 Prediction of triple point trajectory on two-dimensional unsteady shock reflection over single surfaces. *J. Fluid Mech.* **947**, A42.

XIANG, G. & WANG, B. 2017 Numerical study of a planar shock interacting with a cylindrical water column embedded with an air cavity. *J. Fluid Mech.* **825**, 825–852.

XIANG, G. & WANG, B. 2019 Theoretical and numerical studies on shock reflection at water/air two-phase interface: fast-slow case. *Intl J. Multiphase Flow* **114**, 219–228.

YEOM, G.S. & CHANG, K.S. 2013 A modified HLLC-type Riemann solver for the compressible six-equation two-fluid model. *Comput. Fluids* **76**, 86–104.

ZENG, S. & TAKAYAMA, K. 1996 On the refraction of shock wave over a slow-fast gas interface. *Acta Astronaut.* **38** (11), 829–838.

ZHENG, H.W., SHU, C., CHEW, Y.T. & QIN, N. 2011 A solution adaptive simulation of compressible multi-fluid flows with general. *Intl J. Numer. Meth. Fluids* **67**, 616–637.